# Synergistic Effect of Hydrogen Bonding and π-π Stacking Enables Long Cycle Life in Organic Electrode Materials

*Madison R. Tuttle, Shelby T. Davis, and Shiyu Zhang*[*]

Department of Chemistry and Biochemistry, The Ohio State University, 100 West 18th Avenue, Columbus, Ohio 43210, United States

**Corresponding Author**

*zhang.8941@osu.edu

ABSTRACT: Small-molecule organic compounds have emerged as attractive candidates for energy storage in lithium-ion batteries due to their sustainability and modularity. To develop generalizable design principles for organic electrode materials (OEMs), we investigated the correlation between electrochemical performance and addition of functional groups that promote synergistic hydrogen bonding and π-π stacking using a series of quinone-fused aza-phenazines (QAPs) with different hydrogen bonding donor/acceptor arrays. The QAP containing the most hydrogen bonding groups (**3**) exhibits the best performance with discharge capacities of 145 mAh $g^{-1}$ at 2C with 82% capacity retention over 1000 cycles. The performance of **3** is attributed to the strategically incorporated -OH and -$NH_2$ groups, which facilitate strong intermolecular interactions and a tightly packed 2D structure. The intermolecular interaction strength was evaluated using variable temperature 1D $^{1}$H NMR and 2D $^{1}$H-$^{1}$H NOESY, offering a new strategy to help understand and predict the performance of OEMs with hydrogen bonding motifs.

**TOC GRAPHIC**

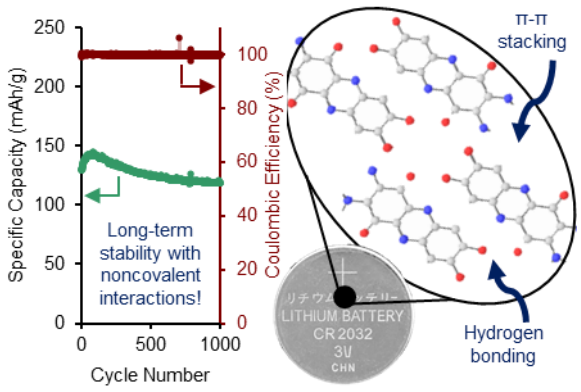

With increasing energy consumption worldwide, there is a growing need to develop efficient and sustainable energy storage devices. Li-ion batteries (LIBs) have been at the forefront of energy storage research since their commercialization in 1991,[1] but current commercial LIBs depend on non-renewable metal oxide or metal phosphate cathodes. Large-scale mining of metal ores is environmentally and economically costly and ultimately unsustainable.[1,2] The rich redox chemistry of organic molecules offers an intriguing alternative to transition metal-based cathode materials,[3–8] as organic electrode materials (OEMs) benefit from abundant starting materials and unparalleled synthetic modularity that allow for systematic optimization of cycling performance. The main challenges for deploying OEMs in LIBs, however, are poor cycle stability and low conductivity, often due to dissolution in electrolyte and inefficient electron transfer between organic charge storage units.

With these issues in mind, our group is interested in developing generalizable design principles for OEMs by exploring the relationship between electrochemical performance and molecular structure. Recently, we demonstrated that S-rich thiazyl heterocycles can facilitate fast, stable redox cycling by reducing the solubility of OEMs through strong intermolecular SOMO-SOMO interactions.[9] However, the thiazyl motifs that enable the strong S···S interactions can be difficult to incorporate into redox-active OEM scaffolds. Therefore, we aim to investigate the correlation between OEM performance and strong intermolecular interactions with more common organic motifs.

We found inspiration in the structure of DNA's double helix, where base pairs form extended non-covalent interaction networks connected by complementary hydrogen bonding (HB) and π-π stacking interactions (Figure 1A). Such interactions stabilize the supramolecular structure, facilitate electron transfer along the DNA double helix,[10,11] and enable DNA's self-assembly[12,13]

and self-repairing[14] properties. In OEMs, introducing moieties that enable either HB or π-π stacking individually have led to promising improvements in performance, such as increased cycle stability in the case of HB[15,16] and enhanced rate capability in the case of π-π stacking.[17–19] Nonetheless, these OEMs exhibit poor capacity retention[15] or sluggish ion kinetics, making their practical application challenging without additional processing.[17,18] We reason that systematically integrating both the stability of HB with the charge transport advantages of π-π stacking together in one scaffold will benefit OEMs by enhancing stability against dissolution, facilitating charge transfer, and providing the structural elasticity required for repeated Li-ion insertion and removal.[20–25]

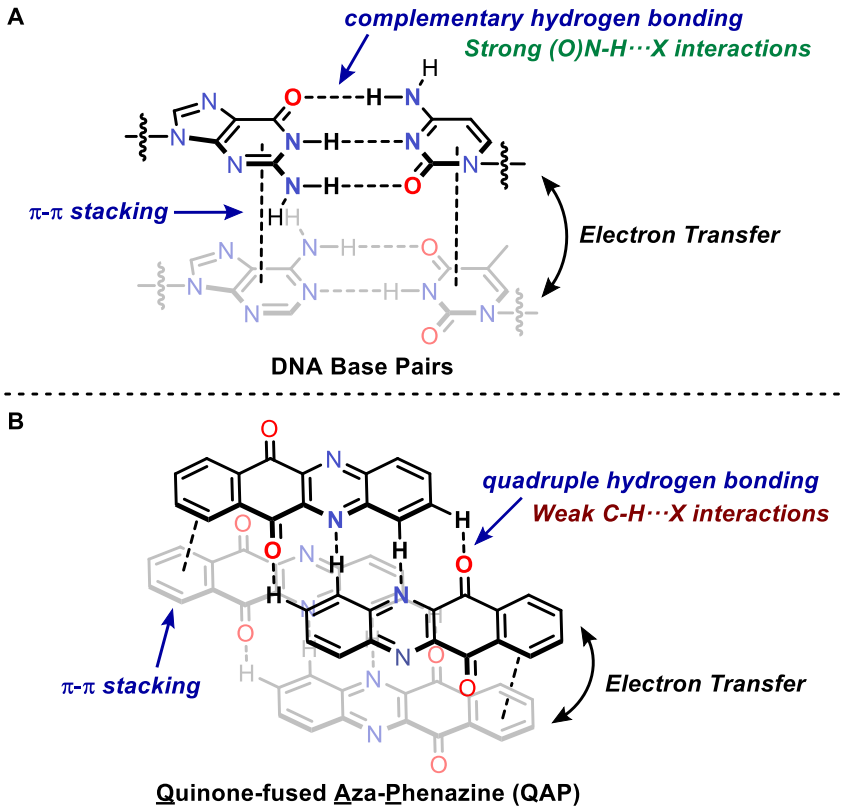


**Figure 1.** (A) Self-assembly of DNA base pairs via the synergistic HB and π–π stacking in DNA can facilitate electron transfer along the longitudinal (π–π stacking) direction. (B) Illustration of

the quadruple HB and π- π stacking in quinone-fused aza-phenazines (QAPs), analogous to the intermolecular interactions observed in DNA.

Similar to DNA, we envisioned that the complementary HB and π-π stacking interactions found in quinone-fused aza-phenazines (QAPs, Figure 1B) could promote a non-covalent interaction network[22,26–28] where electron transfer can occur via connected charge storage units in both longitudinal (π-π stacking) and transverse (HB) directions.[29–35] However, the hydrogen bonds between heteroatomic donors and acceptors in DNA (N-H···X or O-H···X) are much stronger than the weak C-H···X hydrogen bonds in the parent QAP scaffold (Figure 1). Therefore, we hypothesized that QAPs functionalized with additional heteroatomic HB groups, e.g. -OH, -$NH_2$, would exhibit improved performance (e.g. capacity retention and rate capability) over the parent QAP scaffold as a result of enhanced HB interactions. Furthermore, we rationalized that these additional HB groups could serve as meaningful spectroscopic handles to observe and quantify intermolecular interactions, resulting in a useful strategy to help predict the performance of future OEMs with HB motifs.

Herein, we prepared three QAP-based OEMs (**1**-**3**) to understand the synergistic effect of HB and π-π stacking on long-term cycling stability and rate capability. The best performing OEM **3** shows stable cycling at a rate of 2 C for >1000 cycles with a capacity of 145 mAh $g^{-1}$ and 82% capacity retention, rivaling the performance of transition metal-based cathode materials.[36] The intermolecular interactions in **1**-**3** are thoroughly examined and quantified via both solution- and solid-state spectroscopic techniques, offering new strategies to understand and predict the performance of OEMs with HB motifs. In particular, $^1$H NMR and X-ray crystallographic studies reveal that **3** is significantly stabilized by the synergy between -OH and -$NH_2$ groups, ultimately leading to its enhanced performance.

Benzo[b]phenazine-6,11-dione (**1**) was synthesized according to literature procedure via oxidation of the corresponding aza-phenazine with a strong oxidant, $K_2Cr_2O_7$.[27] However, these harsh conditions are intolerant for further derivatization with HB functional groups, e.g. -OH, -$NH_2$. Therefore, we developed a new one-step synthesis of QAP derivatives via the condensation of functionalized *p*-benzoquinones with 2,5-dihydroxy-1,4-benzoquinone (Figure 2A). This method allowed us to quickly develop a series of QAPs (Figure 2B) in good to quantitative yields (68% to 99%). Compounds **1**-**3** were isolated as highly-colored crystalline materials (Figure S6) that are virtually insoluble in most organic solvents and can be easily purified via washing with $H_2O$, MeOH, and acetone. $^{1}H$ and $^{13}C$ NMR, IR, and high-resolution mass spectrometry (HRMS) confirm the structure assignments of **2** and **3** (Figure S3-S4). All QAPs feature a fused, planar π-system and multiple HB groups that facilitate extended π-π stacking and self-complementary HB interactions. In particular, **3** was endowed with both -OH and -$NH_2$ groups as complementary HB motifs, as these heteroatoomic groups can act as both hydrogen bond donors and acceptors.

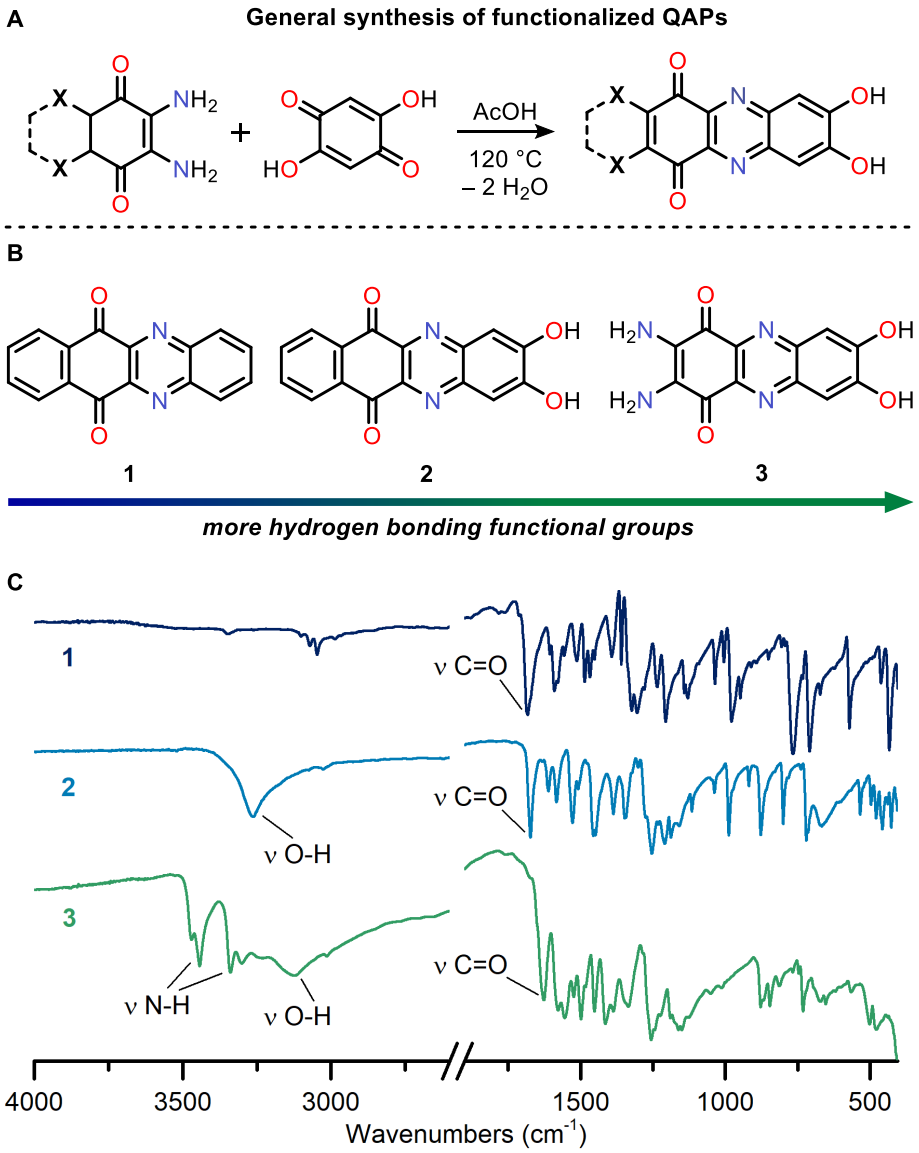


**Figure 2.** (A) Synthesis of functionalized QAPs **2-3** developed in this work. (B) Structures and (C) IR spectra of QAP **1-3** cathode materials employed in this study.

To qualitatively probe the structural stability of the QAP series, we utilized thermogravimetric analysis and differential scanning calorimetry (TGA-DSC). TGA-DSC experiments show that **1** has a melting point of 329 °C, while **2-3** do not melt before decomposition *ca.* 375 °C (Figure S5). These experiments confirm that **2-3** exhibit enhanced structural stability

compared to **1** resulting from incorporation of additional heteroatoomic HB groups. To further compare the strength of HB interactions in **2-3**, we turned to infrared spectroscopy (IR). The IR spectra of **1**-**3** show a shift of the C=O stretching frequency to lower wavenumbers (1682 $cm^{-1}$ in **1**, 1673 $cm^{-1}$ in **2**, 1628 $cm^{-1}$ in **3**, Figure 2C). Such a red-shifting trend is consistent with weakening of the C=O bond as the HB interactions (C=O···H-X) increase.[15] A shift of the O–H stretching frequency from 3260 $cm^{-1}$ in **2** to 3119 $cm^{-1}$ in **3** further demonstrates the enhanced intermolecular interaction network of **3** over **2** (Figure 2C).

We examined the redox abilities of **1**-**3** by solution cyclic voltammetry (supplemental pg. S16). The cyclic voltammogram (CV) of **1** shows characteristic quinone behavior with two single-electron redox couples at −1.05 V and −1.08 V (vs. $Ag^{+}/Ag$, Figure S10). In contrast, **2**-**3** exhibit more complex electrochemistry that suggests redox-responsive proton transfer from the catechol moiety to the quinone (Figure S10, supplemental pg. S17).[37] To probe our hypothesis, we performed CV measurements of **1** in the presence of catechol, which reveals quasi-reversible redox features similar to **2-3** (Figure S11). Additional scan-rate-dependent CV measurements on solutions of **1** in the presence of catechol and **2**-**3** showed that the reduction and oxidation processes involve *ca.* two electrons (Figure S12), consistent with our proton transfer hypothesis. These findings are similar to those of Smith and coworkers, indicating that **2**-**3** exhibit self-associative HB even at low concentrations in polar solvents.

The electrochemical properties of **1**-**3** in solid-state were evaluated in coin-type cells (supplemental pg. S20). Unlike in solution, molecules of **1-3** in solid-state are locked in place in the crystal lattice, preventing complete proton transfer during redox. As a result, solid-state CV measurements of Li-QAP cells at 0.1 mV $s^{-1}$ show clear semiquinone (0/•−) and quinone (•−/$2^{-}$)

redox couples centered at 2.67 V for **1**, 2.45 V and 2.36 V for **2**, and 2.60 V and 2.26 V for **3** (vs. $Li^+/Li$, Figure 3A, Figure S13).

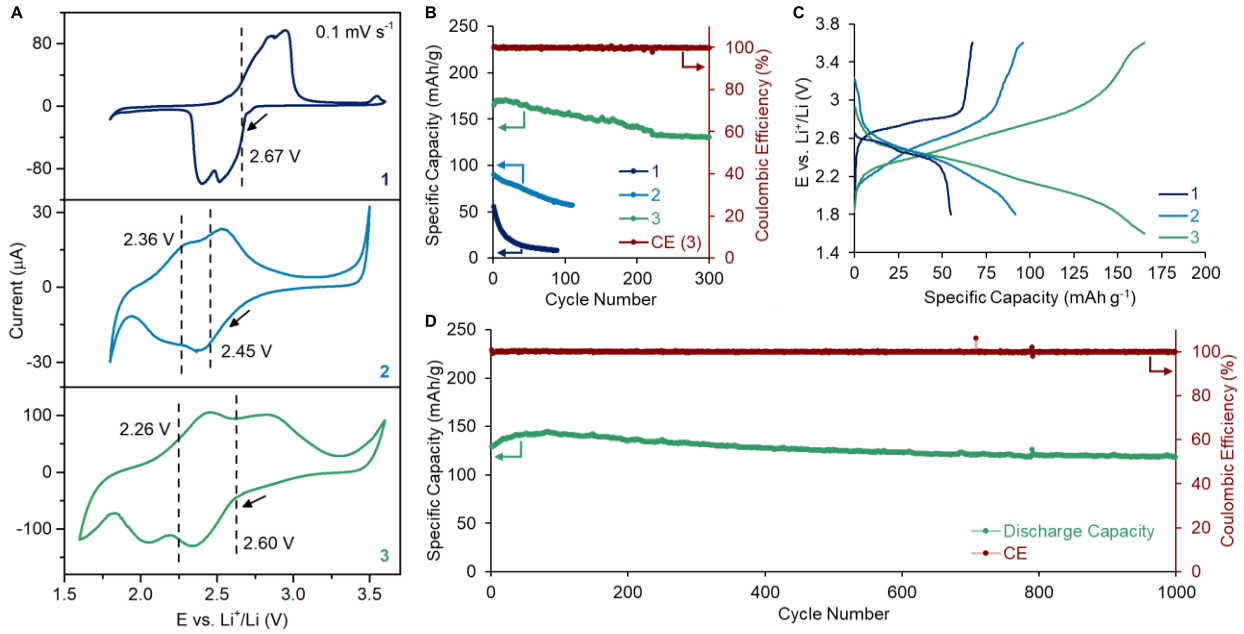


**Figure 3.** (A) Solid-state CV data of **1-3** at a scan rate of 0.1 mV $s^{-1}$. (B) Galvanostatic cycling comparison of **1-3** at a rate of 1C. The priming period cycles are removed for clarity. (C) Voltage profile of the first cycles of **1-3** following the priming period. (D) Long-term galvanostatic cycling of **3** at a rate of 2C. The priming period cycles are removed for clarity.

To elucidate how HB and π-π stacking intermolecular interactions affect the electrochemical performance of **1-3**, galvanostatic charge-discharge experiments were performed at a two-electron per molecule level with voltage cut-offs (3.6–1.8V for **1-2** and 3.6–1.6V for **3**) selected based on solid-state CV studies (vide supra). A priming period of ten cycles at 0.5C was performed before the cell was cycled at 1C. Li cells of **1-2** ($C_{theo}$: 206 mAh $g^{-1}$ and 183 mAh $g^{-1}$) deliver discharge capacities at 27% and 49%, respectively, of theoretical two-electron values at 1C (206 mA $g^{-1}$ and 183 mA $g^{-1}$, Figure 3B), which continue to fade to <5% and <35% in subsequent cycles. The charge-discharge profiles of **1-2** exhibit a sloping two-step plateau (2.56

V and 2.40 V vs. $Li^+/Li$) and a continuous slope (Figure 3C), respectively, consistent with the solid-state CVs (Figure 3A, Figures S13-S15). The first few cycles of **1**-**2** (Figure S14-S15) show Coulombic efficiencies *ca.* 85% and 90%, respectively, suggesting **1-2** may undergo self-discharge due to dissolution.[38–43] Visual inspection of the disassembled coin-type cells of **1**-**2** reveals highly-colored Celgard separators and Li anode surfaces, confirming the dissolution of **1**-**2** during cycling (Figure S18).

In contrast, Li-**3** cells ($C_{theo}$: 197 mAh $g^{-1}$) deliver high discharge capacities of *ca.* 169 mAh $g^{-1}$ at 1C (197 mA $g^{-1}$, Figure 3B) with a continuous charge-discharge profile (Figure 3C, Figure S16). The capacity remains stable over 1000 cycles with Coulombic efficiencies >99% (Figure S16). The disassembled Li-**3** cell showed no signs of dissolution after 1000 cycles (Figure S18). Notably, rate capability experiments with **3** show excellent capacity retention even at very high rates of 10C (1970 mA $g^{-1}$, Figure S16), and capacities up to 174 mAh $g^{-1}$ are recovered after returning to 1C. In long-term stability studies at a lower rate of 0.5C, **3** can reach a discharge capacity of 183 mAh $g^{-1}$ with 84% capacity retention over 500 cycles (Figure S17). Remarkably, even at higher rates of 2C (394 mA $g^{-1}$), **3** can reach discharge capacities of 145 mAh $g^{-1}$ with 82% capacity retention over 1000 cycles (Figure 3D, Figure S17). With excellent cycle stability and rate capability, **3** drastically outperforms **1** and **2**, as well as many other quinone-based OEMs.[1,3–8]

To understand the structural features of **3** that enable its enhanced galvanostatic cycling, the solid-state structure of **3** was studied by powder X-ray diffraction (PXRD) at the Advanced Photon Source (Chicago, IL, $\lambda$ = 0.4569 Å). Rietveld refinement of the PXRD data using GSAS-II software[44] revealed that **3** packs in a $P2_1/n$ space group with a unit cell volume of 1045 $Å^3$ ($Z$ = 4). Molecules of **3** assemble into $\pi$-stacked columns (along $c$ axis, stacking distance: *ca.* 3.41 Å,

Figure 4A). Four π-stacked columns are connected via alternating O-H···$N_{Ar}$ (1.847 Å), O-H···O=C (2.041 Å), N-H···O=C (2.227 Å), and N-H···OH (1.946 Å) interactions to form a tetrameric cyclic structure (Figure 4A), showcasing the necessity of the -OH and -$NH_2$ groups to create a stable structure. Additional inter- and intramolecular N-H···O=C interactions (2.154 Å and 2.227 Å, respectively) connect the tetrameric columns of **3** in an extended layer structure (Figure S8-S9). While the solid structure of **1** is dominated by long, weak C-H···$N_{Ar}$ interactions (Figure 4B, 2.682 and 2.668 Å), the synergistic π-π stacking and short, strong (O)N-H···X interactions in **3** results in more tightly packed columns reminiscent of DNA's double helix.

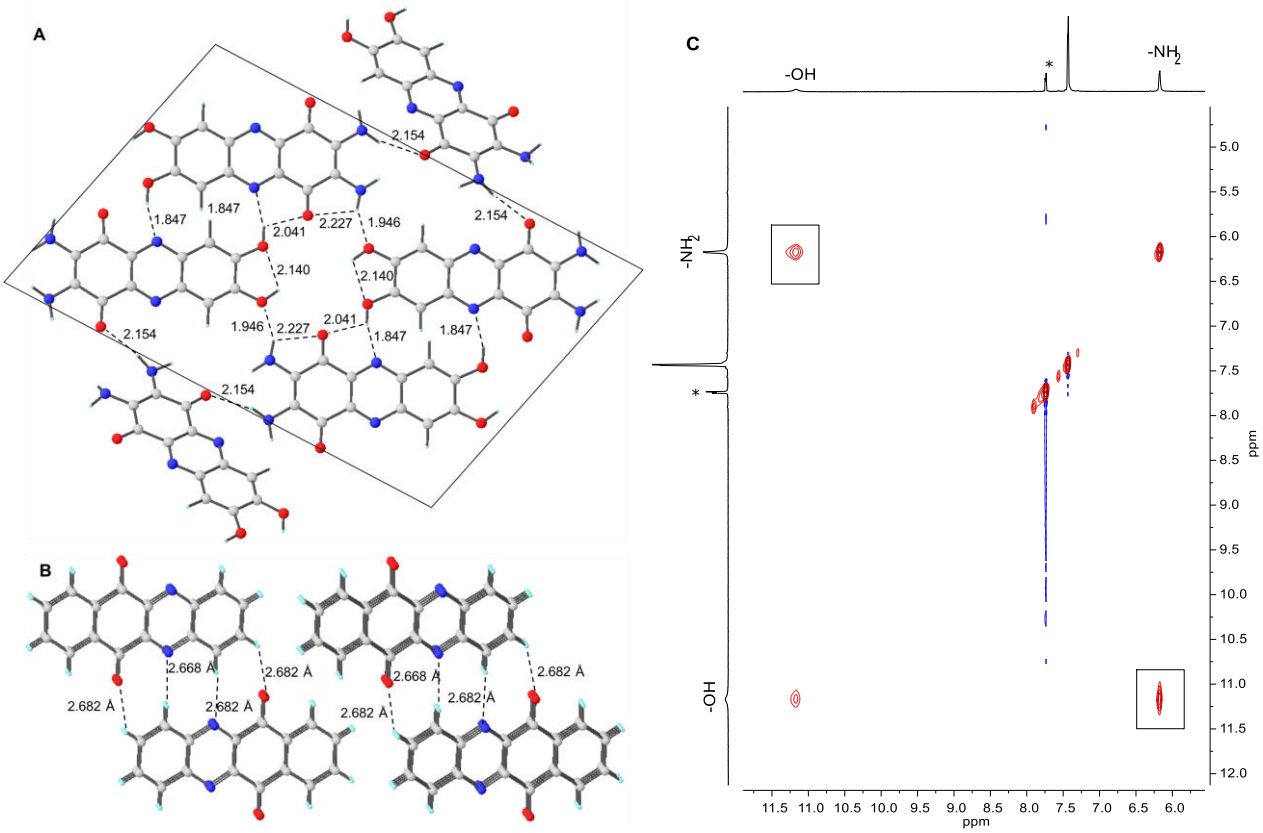


**Figure 4.** Solid-state structures of (A) **3** determined by Rietveld refinement and (B) **1** by single-crysal diffraction (CCDC: 761662). A H-bonded tetramer of **3** is highlighted with a black box. Only one layer of **3** is shown for clarity. (C) 2D $^{1}$H-$^{1}$H NOESY spectrum of **3**. Cross peaks between -OH and -$NH_2$ signals are highlighted with black boxes. The residual peak of $C_6D_6$ is markedy by an asterisk.

Variable temperature NMR spectroscopy (VT-NMR) has been widely used to investigate intermolecular interactions in solution.[45] With the HB groups (e.g. -CH, -OH, and -$NH_2$) in **1-3** as spectroscopic handles, we employed VT-NMR to quantify the strength of intermolecular interactions in solution, which can include both HB and π-π stacking.[46–48] If self-association occurs in solution, the chemical shifts of protons will shift as a function of solution temperature ($\Delta\delta/\Delta T$),[49,50] providing insight into the thermodynamics of intermolecular interactions and the supramolecular organization of **1-3**. The $^1$H NMR chemical shifts of **1** remain constant from 27 °C to 70 °C in a 5:4 mixture of DMSO-$d_6$ and benzene-$d_6$, suggesting that compound **1** exists exclusively as monomers in solution (Figure S19, supplemental pg. S26). In contrast, the -OH and -$NH_2$ chemical shifts of **2-3** show a strong temperature dependence (Figure S20-S24), as summarized in Table 1. Thermodyanamic parameters associated with the equilibria between hydrogen-bonded and a non-hydrogen-bonded states were extracted by van't Hoff analysis (supplemental pg. S30, Figures S23-S24), and the resulting $\Delta H$ and $\Delta S$ values for each functional group are summarized in Table 1. As expected, the self-association of **2-3** is enthalpically favored ($\Delta H < 0$) and entropically disfavored ($\Delta S < 0$). In particular, the van't Hoff analysis for **3** shows that both -OH and -$NH_2$ groups engage in substantial HB interactions (*ca.* 24 – 27 kcal mol$^{-1}$) that may involve arrays of multiple donors and acceptors.[51,52] It is interesting to note that the enthalpies of HB for different functional groups are essentially the same (~26 kcal mol$^{-1}$) for both **2** and **3** (Table 1). Therefore, we reason that the significantly higher stability of **3** over **2** should be, at least partially, attributed to the synergy of -OH and -$NH_2$. To further probe this hypothesis, we employed $^1$H-$^1$H NOESY (nuclear Overhauser effect spectroscopy) to investigate the interactions of -OH and -$NH_2$ groups in solutions of **3**. Indeed, a positive NOE cross peak between the -OH and -$NH_2$ chemical shifts is observed (Figure 4C, Figure S25), indicating a direct intermolecular HB

interaction between the -OH and -$NH_2$ groups of **3**.[53–55] These observations nicely corroborate the solid structure of **3** (vide supra) and confirm that the synergy between -OH and -$NH_2$ groups is essential for stabilizing the supramolecular structure of **3**.

**Table 1.** Calculated temperature dependences and thermodynamic parameters of **1**-**3** based on VT-NMR and van't Hoff analysis.

| Compound | $\Delta\delta/\Delta T$ (ppm $K^{-1}$) | $\Delta H°$ (kcal $mol^{-1}$) | $\Delta S°$ (cal $mol^{-1}$ $K^{-1}$) |
|---|---|---|---|
| **1** | 0 | – | – |
| **2** (-OH) | $-6.1 \times 10^{-3}$ | –27.66 ± 3.817 | –84.92 ± 11.995 |
| **3** (-OH) | $-6.0 \times 10^{-3}$ | –24.99 ± 2.150 | –77.22 ± 6.756 |
| **3** (-$NH_2$) | $-4.2 \times 10^{-3}$ | –26.83 ± 3.610 | –82.29 ± 11.342 |

In conclusion, our study elucidates a network of synergistic noncovalent forces that stabilize the QAP-based OEM **3** and facilitate its excellent performance in Li-ion batteries with discharge capacities of up to 145 mAh $g^{-1}$ at 2C and 82% capacity retention over 1000 cycles. We found that the inclusion of heteroatomic HB groups, e.g. -OH and -$NH_2$, is crucial for electrode stability. Importantly, the stabilizing effect of HB groups on improving OEM performance is additive, providing a design strategy that is potentially applicable to other OEMs. As disruption of HB and other noncovalent interactions must occur on the battery cycling time-scale, it is necessary to consider the energetic favorability of intermolecular interactions in both solution and solid-state. We demonstrated that both $^1$H NMR and X-ray crystallographic studies of **3** were key in understanding the synergistic effect of HB groups and π-π stacking on OEM cycling stability. Furthermore, the combination of 1D VT-NMR and 2D NOESY techniques provides a

straightforward approach to understand and potentially predict the cycling stability of future OEMs with HB motifs.

## ASSOCIATED CONTENT

### Supporting Information

Experimental details, synthetic procedures, electrochemical details, crystallographic and refinement details, NMR details, including Figure S1-S25.

## AUTHOR INFORMATION

https://research.cbc.osu.edu/zhang.8941/

@ZhangLabOSU

### Notes

The authors declare no competing financial interests.

## ACKNOWLEDGMENTS

This work was supported in part through the National Science Foundation Graduate Research Fellowship under Grant No. DGE-1343012. The authors would like to thank beyond measure the following scientists whose skill and excellence made this work possible during a global pandemic: Weiyao Zhang for VT-NMR; Warren Huey and the Goldberger Lab for TGA-DSC; the Wade and McGrier labs for ATR-IR; Dr. Curtis Moore for PXRD; Dr. Alicia Friedman for HRMS; Tanya Whitmer and Dan Conroy for NMR and 2D NOESY; Prof. Casey Wade and Prof. Pat Woodward for Rietveld refinement of **3**. Use of the Advanced Photon Source at Argonne National Laboratory

was supported by the U. S. Department of Energy, Office of Science, Office of Basic Energy Sciences, under Contract No. DE-AC02-06CH11357

REFERENCES

(1) Larcher, D.; Tarascon, J.-M. Towards Greener and More Sustainable Batteries for Electrical Energy Storage. *Nat. Chem.* **2015**, *7*, 19.

(2) Gaines, L. The Future of Automotive Lithium-Ion Battery Recycling: Charting a Sustainable Course. *Sustain. Mater. Technol.* **2014**, *1*, 2.

(3) Bhosale, M. E.; Chae, S.; Kim, J. M.; Choi, J.-Y. Organic Small Molecules and Polymers as an Electrode Material for Rechargeable Lithium Ion Batteries. *J. Mater. Chem. A* **2018**, *6*, 19885.

(4) Schon, T. B.; McAllister, B. T.; Li, P.-F.; Seferos, D. S. The Rise of Organic Electrode Materials for Energy Storage. *Chem. Soc. Rev.* **2016**, *45*, 6345.

(5) Muench, S.; Wild, A.; Friebe, C.; Häupler, B.; Janoschka, T.; Schubert, U. S. Polymer-Based Organic Batteries. *Chem. Rev.* **2016**, *116*, 9438.

(6) Wu, Y.; Zeng, R.; Nan, J.; Shu, D.; Qiu, Y.; Chou, S.-L. Quinone Electrode Materials for Rechargeable Lithium/Sodium Ion Batteries. *Adv. Energy Mater.* **2017**, *7*, 1700278.

(7) Lee, S.; Kwon, G.; Ku, K.; Yoon, K.; Jung, S.-K.; Lim, H.-D.; Kang, K. Recent Progress in Organic Electrodes for Li and Na Rechargeable Batteries. *Adv. Mater.* **2018**, *30*, 1704682.

(8) Häupler, B.; Wild, A.; Schubert, U. S. Carbonyls: Powerful Organic Materials for Secondary Batteries. *Adv. Energy Mater.* **2015**, *5*, 1402034.

(9) Tuttle, M. R.; Zhang, S. Bisthiazolyl Quinones: Stabilizing Organic Electrode Materials with Sulfur-Rich Thiazyl Motifs. *Chem. Mater.* **2020**, *32*, 255.

(10) Watson, J. D.; Crick, F. H. C. Molecular Structure of Nucleic Acids: A Structure for Deoxyribose Nucleic Acid. *Nature* **1953**, *171*, 737.

(11) Sontz, P. A.; Muren, N. B.; Barton, J. K. DNA Charge Transport for Sensing and Signaling. *Acc. Chem. Res.* **2012**, *45*, 1792.

(12) Li, Z.; Wang, J.; Li, Y.; Liu, X.; Yuan, Q. Self-Assembled DNA Nanomaterials with Highly Programmed Structures and Functions. *Materials Chemistry Frontiers* **2018**, *2*, 423.

(13) Yang, D.; Campolongo, M,. J.; Nhi Tran, T. N.; Ruiz, R. C. H.; Kahn, J. S.; Luo, D. Novel DNA Materials and Their Applications. *Wiley Interdiscip. Rev. Nanomedicine Nanobiotechnology* **2010**, *2*, 648.

(14) Li, Y.; Schulman, R. DNA Nanostructures That Self-Heal in Serum. *Nano Lett.* **2019**, *19*, 3751.

(15) Sieuw, L.; Jouhara, A.; Quarez, É.; Auger, C.; Gohy, J. F.; Poizot, P.; Vlad, A. A H-Bond Stabilized Quinone Electrode Material for Li-Organic Batteries: The Strength of Weak Bonds. *Chem. Sci.* **2019**, *10*, 418.

(16) Tian, B.; Ding, Z.; Ning, G. H.; Tang, W.; Peng, C.; Liu, B.; Su, J.; Su, C.; Loh, K. P. Amino Group Enhanced Phenazine Derivatives as Electrode Materials for Lithium Storage. *Chem. Commun.* **2017**, *53*, 2914.

(17) Lei, Z.; Chen, X.; Sun, W.; Zhang, Y.; Wang, Y. Exfoliated Triazine-Based Covalent Organic Nanosheets with Multielectron Redox for High-Performance Lithium Organic

Batteries. *Adv. Energy Mater.* **2019**, *9*, 1801010.

(18) Wang, S.; Wang, Q.; Shao, P.; Han, Y.; Gao, X.; Ma, L.; Yuan, S.; Ma, X.; Zhou, J.; Feng, X.; et al. Exfoliation of Covalent Organic Frameworks into Few-Layer Redox-Active Nanosheets as Cathode Materials for Lithium-Ion Batteries. *J. Am. Chem. Soc.* **2017**, *139*, 4258.

(19) Wang, M.; Guo, H.; Xue, R.; Li, Q.; Liu, H.; Wu, N.; Yao, W.; Yang, W. Covalent Organic Frameworks: A New Class of Porous Organic Frameworks for Supercapacitor Electrodes. *ChemElectroChem* **2019**, *6*, 2984.

(20) Wojtecki, R. J.; Meador, M. A.; Rowan, S. J. Using the Dynamic Bond to Access Macroscopically Responsive Structurally Dynamic Polymers. *Nat. Mater.* **2011**, *10*, 14.

(21) Burattini, S.; Colquhoun, H. M.; Fox, J. D.; Friedmann, D.; Greenland, B. W.; Harris, P. J. F.; Hayes, W.; MacKay, M. E.; Rowan, S. J. A Self-Repairing, Supramolecular Polymer System: Healability as a Consequence of Donor-Acceptor π-π Stacking Interactions. *Chem. Commun.* **2009**, *44*, 6717.

(22) Steiner, T. The Hydrogen Bond in the Solid State. *Angew. Chemie Int. Ed.* **2002**, *41*, 48.

(23) Zhou, B.; He, D.; Hu, J.; Ye, Y.; Peng, H.; Zhou, X.; Xie, X.; Xue, Z. A Flexible, Self-Healing and Highly Stretchable Polymer Electrolyte via Quadruple Hydrogen Bonding for Lithium-Ion Batteries. *J. Mater. Chem. A* **2018**, *6*, 11725.

(24) Wang, C.; Wu, H.; Chen, Z.; McDowell, M. T.; Cui, Y.; Bao, Z. Self-Healing Chemistry Enables the Stable Operation of Silicon Microparticle Anodes for High-Energy Lithium-Ion Batteries. *Nat. Chem.* **2013**, *5*, 1042.

(25) Luo, C.; Fan, X.; Ma, Z.; Gao, T.; Wang, C. Self-Healing Chemistry between Organic Material and Binder for Stable Sodium-Ion Batteries. *Chem* **2017**, *3*, 1050.

(26) Miao, S.; Brombosz, S. M.; Schleyer, P. V. R.; Wu, J. I.; Barlow, S.; Marder, S. R.; Hardcastle, K. I.; Bunz, U. H. F. Are N,N-Dihydrodiazatetracene Derivatives Antiaromatic? *J. Am. Chem. Soc.* **2008**, *130*, 7339.

(27) Tang, Q.; Liang, Z.; Liu, J.; Xu, J.; Miao, Q. N-Heteroquinones: Quadruple Weak Hydrogen Bonds and n-Channel Transistors. *Chem. Commun.* **2010**, *46*, 2977.

(28) Vitaku, E.; Gannett, C. N.; Carpenter, K. L.; Shen, L.; Abruña, H. D.; Dichtel, W. R. Phenazine-Based Covalent Organic Framework Cathode Materials with High Energy and Power Densities. *J. Am. Chem. Soc.* **2020**, *142*, 16.

(29) Neilands, O.; Tilika, V.; Sudmale, I.; Grigorjeva, I.; Edzina, A.; Fonavs, E.; Muzikante, I. Dioxo- and Aminooxopyrimidotetrathiafulvalenes: π-Electron Donors for Design of Conducting Materials Containing Intramolecular Hydrogen Bonds of Nucleic Acid Base Pair Type. *Adv. Mater. Opt. Electron.* **1997**, *7*, 39.

(30) Ueda, A.; Yamada, S.; Isono, T.; Kamo, H.; Nakao, A.; Kumai, R.; Nakao, H.; Murakami, Y.; Yamamoto, K.; Nishio, Y.; et al. Hydrogen-Bond-Dynamics-Based Switching of Conductivity and Magnetism: A Phase Transition Caused by Deuterium and Electron Transfer in a Hydrogen-Bonded Purely Organic Conductor Crystal. *J. Am. Chem. Soc.* **2014**, *136*, 12184.

(31) González-Rodríguez, D.; Schenning, A. P. H. J. Hydrogen-Bonded Supramolecular π-Functional Materials. *Chem. Mater.* **2011**, *23*, 310.

(32) Yoshioka, M.; Saigo, K.; Ogura, T.; Kobayashi, Y.; Hashizume, D. Hydrogen-Bonding-Assisted Self-Doping in Tetrathiafulvalene (TTF) Conductor. *J. Am. Chem. Soc.* **2009**, *131*, 9995.

(33) Murata, T.; Morita, Y.; Fukui, K.; Sato, K.; Shiomi, D.; Takui, T.; Maesato, M.; Yamochi, H.; Saito, G.; Nakasuji, K. A Purely Organic Molecular Metal Based on a Hydrogen-Bonded Charge-Transfer Complex: Crystal Structure and Electronic Properties of TTF-Imidazole-p-Chloranil. *Angew. Chemie Int. Ed.* **2004**, *43*, 6343.

(34) El-Ghayoury, A.; Mézière, C.; Simonov, S.; Zorina, L.; Cobián, M.; Canadell, E.; Rovira, C.; Náfrádi, B.; Sipos, B.; Forró, L.; et al. A Neutral Zwitterionic Molecular Solid. *Chem. - A Eur. J.* **2010**, *16*, 14051.

(35) Balodis, K.; Khasanov, S.; Chong, C.; Maesato, M.; Yamochi, H.; Saito, G.; Neilands, O. Single Component Betainic Conductor: Pyrimido-Fused TTF Derivatives Having Ethylenedioxy Group. *Synth. Met.* **2003**, *133*, 353.

(36) Nitta, N.; Wu, F.; Lee, J. T.; Yushin, G. Li-Ion Battery Materials: Present and Future. *Mater. Today* **2015**, *18*, 252.

(37) Ge, Y.; Miller, L.; Ouimet, T.; Smith, D. K. Electrochemically Controlled Hydrogen Bonding. O-Quinones as Simple Redox-Dependent Receptors for Arylureas. *J. Org. Chem.* **2000**, *65*, 8831.

(38) Xie, J.; Zhang, Q. Recent Progress in Rechargeable Lithium Batteries with Organic Materials as Promising Electrodes. *J. Mater. Chem. A* **2016**, *4*, 7091.

(39) Yokoji, T.; Kameyama, Y.; Maruyama, N.; Matsubara, H. High-Capacity Organic Cathode

Active Materials of 2,2′-Bis-p-Benzoquinone Derivatives for Rechargeable Batteries. *J. Mater. Chem. A* **2016**, *4*, 5457.

(40) Liang, Y.; Tao, Z.; Chen, J. Organic Electrode Materials for Rechargeable Lithium Batteries. *Adv. Energy Mater.* **2012**, *2*, 742.

(41) Sun, M.; Wang, X.; Wang, J.; Yang, H.; Wang, L.; Liu, T. Assessment on the Self-Discharge Behavior of Lithium-Sulfur Batteries with LiNO 3 -Possessing Electrolytes. *ACS Appl. Mater. Interfaces* **2018**, *10*, 35175.

(42) Lacey, M. J.; Yalamanchili, A.; Maibach, J.; Tengstedt, C.; Edström, K.; Brandell, D. The Li–S Battery: An Investigation of Redox Shuttle and Self-Discharge Behaviour with LiNO $_3$ -Containing Electrolytes. *RSC Adv.* **2016**, *6*, 3632.

(43) Sevov, C. S.; Hendriks, K. H.; Sanford, M. S. Low-Potential Pyridinium Anolyte for Aqueous Redox Flow Batteries. *J. Phys. Chem. C* **2017**, *121*, 24376.

(44) Toby, B. H.; Von Dreele, R. B. {\it GSAS-II}: The Genesis of a Modern Open-Source All Purpose Crystallography Software Package. *J. Appl. Crystallogr.* **2013**, *46*, 544.

(45) Morton, J. G.; Joe, C. L.; Stolla, M. C.; Koshland, S. R.; Londergan, C. H.; Schofield, M. H. NMR Determination of Hydrogen Bond Thermodynamics in a Simple Diamide: A Physical Chemistry Experiment. *J. Chem. Educ.* **2015**, *92*, 1086.

(46) Shetty, A. S.; Zhang, J.; Moore, J. S. Aromatic π-Stacking in Solution as Revealed through the Aggregation of Phenylacetylene Macrocycles. *J. Am. Chem. Soc.* **1996**, *118*, 1019.

(47) Parenti, F.; Tassinari, F.; Libertini, E.; Lanzi, M.; Mucci, A. π-Stacking Signature in NMR Solution Spectra of Thiophene-Based Conjugated Polymers. *ACS omega* **2017**, *2*, 5775.

(48) White, L. J.; Wells, N. J.; Blackholly, L. R.; Shepherd, H. J.; Wilson, B.; Bustone, G. P.; Runacres, T. J.; Hiscock, J. R. Towards Quantifying the Role of Hydrogen Bonding within Amphiphile Self-Association and Resultant Aggregate Formation. *Chem. Sci.* **2017**, *8*, 7620.

(49) Schofield, M. H.; Morton, J. G.; Koshland, S. R.; Joe, C. L.; Londergan, C. H.; Stolla, M. C. NMR Determination of Hydrogen Bond Thermodynamics in a Simple Diamide: A Physical Chemistry Experiment. *J. Chem. Educ.* **2015**, *92*, 1086.

(50) Gellman, S. H.; Dado, G. P.; Liang, G. B.; Adams, B. R. Conformation-Directing Effects of a Single Intramolecular Amide-Amide Hydrogen Bond: Variable-Temperature NMR and IR Studies on a Homologous Diamide Series. *J. Am. Chem. Soc.* **1991**, *113*, 1164.

(51) Li, J.; Wisner, J. A.; Jennings, M. C. A Self-Associating ADADA Hydrogen-Bonded Double Helix. *Org. Lett.* **2007**, *9*, 3267.

(52) Drain, C. M.; Shi, X.; Milic, T.; Nifiatis, F. Self-Assembled Multiporphyrin Arrays Mediated by Self-Complementary Quadruple Hydrogen Bond Motifs. *Chem. Commun.* **2001**, *3*, 287.

(53) Mann, S. K.; Pham, T. N.; McQueen, L. L.; Lewandowski, J. R.; Brown, S. P. Revealing Intermolecular Hydrogen Bonding Structure and Dynamics in a Deep Eutectic Pharmaceutical by Magic-Angle Spinning NMR Spectroscopy. *Mol. Pharm.* **2020**, *17*, 622.

(54) Mogck, O.; Pons, M.; Böhmer, V.; Vogt, W. NMR Studies of the Reversible Dimerization and Guest Exchange Processes of Tetra Urea Calix[4]Arenes Using a Derivative with Lower Symmetry. *J. Am. Chem. Soc.* **1997**, *119*, 5706.

(55) Charisiadis, P.; Kontogianni, V. G.; Tsiafoulis, C. G.; Tzakos, A. G.; Siskos, M.; Gerothanassis, I. P. 1H-NMR as a Structural and Analytical Tool of Intra- and Intermolecular Hydrogen Bonds of Phenol-Containing Natural Products and Model Compounds. *Molecules*. **2014**, *19*, 13643.

Electronic Supporting Information for:

**Synergistic Effect of Hydrogen Bonding and π-π Stacking Enables Long Cycle Life in Organic Electrode Materials**

Madison R. Tuttle, Shelby T. Davis, and Shiyu Zhang*

Department of Chemistry and Biochemistry, The Ohio State University, 100 West 18th Avenue, Columbus, Ohio 43210, United States

## Contents

## General Experimental Details

All experiments were carried out under nitrogen (or argon) atmosphere using an MBraun glovebox and/or standard Schlenk techniques unless stated otherwise. $^{1}H$ and $^{13}C$ NMR spectra were recorded on Bruker 400 or 600 MHz spectrometer and were externally referenced to the NMR residual solvent peaks. ATR-IR spectra were measured using a Nicolet IR 200 with a diamond ATR accessory. Thermogravimetric analysis (TGA) and differential scanning calorimetry (DSC) experiments were carried out under nitrogen with a TA Instruments Discovery SDT 650 using a heating rate of 3 °C $min^{-1}$ between 50 and 600 °C. Cyclic voltammetry and potentio-electrochemical impedance spectroscopy experiments were performed with a Biologic SP-150 single-channel potentiostat. Galvanostatic cycling experiments were performed with a LAND CT2001A battery testing system. Unless otherwise noted, all solvents were degassed and dried using a Pure Process Technology (PPT) solvent purification system and stored under an atmosphere of nitrogen over 4 Å molecular sieves. DMSO-$d_6$ and $C_6D_6$ (Cambridge Isotope Labs) were dried over $CaH_2$ and vacuum transferred onto 4 Å molecular sieves prior to use. All glassware were dried at 175 °C before use. All reagents were purchased from Sigma Aldrich unless otherwise noted.

## Preparation and Characterization of Compounds

**Scheme S1.** Synthesis of **1**

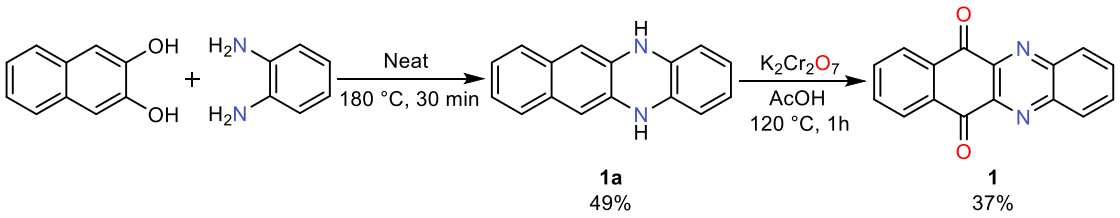


### Synthesis and characterization of 5,12-dihydrobenzo[b]phenazine (1a)

5,12-dihydrobenzo[b]phenazine was prepared according to a modified literature procedure.[1] In a roundbottom flask, a neat mixture of o-phenylenediamine (0.600 g, 5.55 mmol) and naphthalene-2,3-diol (0.889 g, 5.55 mmol) was mixed with stirring. The mixture was heated to 180 °C and stirred for 30 minutes. After cooling to room temperature, the resulting black solid was transferred to a glass frit and washed with methanol, acetone, and diethyl ether. The resulting material was collected and dried *in vacuo* at 90 °C overnight to give the product as a tan solid (0.632 g, 49%). $^{1}H$ NMR (DMSO-$d_6$, 400 MHz): δ 8.11 (s, 2H), δ 7.15 (m, 2H), δ 6.92 (m, 2H), δ 6.34 (m, 2H), δ 6.24 (s, 2H), δ 6.18 (m, 2H). The $^{1}H$ NMR spectrum of the product matches that reported in the literature.[1]

**Synthesis and characterization of benzo[b]phenazine-6,11-dione (1)**

Benzo[b]phenazine-6,11-dione was prepared according to a modified literature procedure.[2] To a roundbottom flask charged with a warm (60 °C) solution of 5,12-dihydrobenzo[b]phenazine (**1a**, 0.300 g, 1.29 mmol) in acetic acid (40 mL), $K_2Cr_2O_7$ (1.29 g, 4.39 mmol) was added. The solution was stirred at reflux (120 °C) for one hour, turning dark green. After cooling to room temperature, acetone (20 mL) was added to the green solution, resulting in precipitation of a yellow crystalline solid. This solid was filtered, washing with acetone until the filtrate was clear, and dried *in vacuo* at 90 °C overnight to yield the product as a dark yellow crystalline solid (0.124 g, 37%). mp: 329 °C with decomposition (Figure S5). $^1$H NMR (DMSO-$d_6$, 400 MHz): δ 8.41 (dd, $J_1$=6.36 Hz, $J_2$=3.49 Hz, 2H), δ 8.34 (dd, $J_1$=5.73 Hz, $J_2$=3.39 Hz, 2H), δ 8.15 (dd, $J_1$=6.41 Hz, $J_2$=3.40 Hz, 2H), δ 8.03 (dd, $J_1$=5.92 Hz, $J_2$=3.26 Hz, 2H). $^{13}$C NMR (DMSO-$d_6$, 100 MHz): δ 181.4, δ 145.7, δ 143.1, δ 135.3, δ 134.0, δ 130.9, δ 127.7. IR (ATR, cm$^{-1}$): 3100, 3071, 3046, 1682, 1597, 1590, 1577, 1556, 1489, 1486, 1468, 1452, 1392, 1337, 1323, 1304, 1213, 1206, 1132, 1129, 1036, 986, 978, 967, 931, 909, 850, 785, 766, 709, 672, 571, 440, 433 (Figure S1). The $^1$H and $^{13}$C NMR spectra of the product matches that reported in the literature.[2]

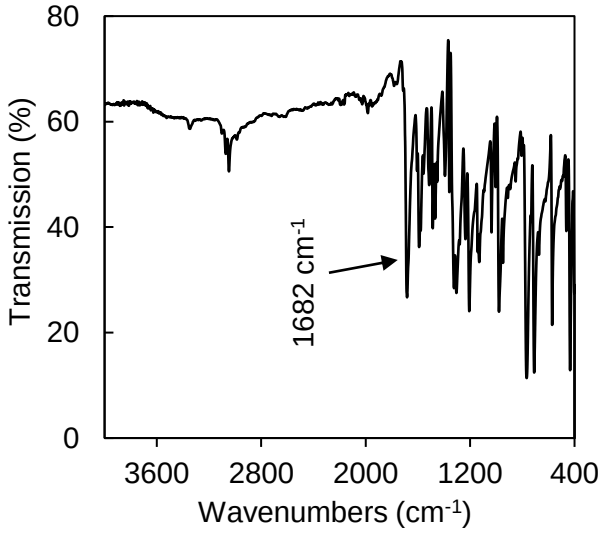


**Figure S1.** IR (ATR) spectra of benzo[b]phenazine-6,11-dione (**1**).

**Scheme S2.** Synthesis of **2**

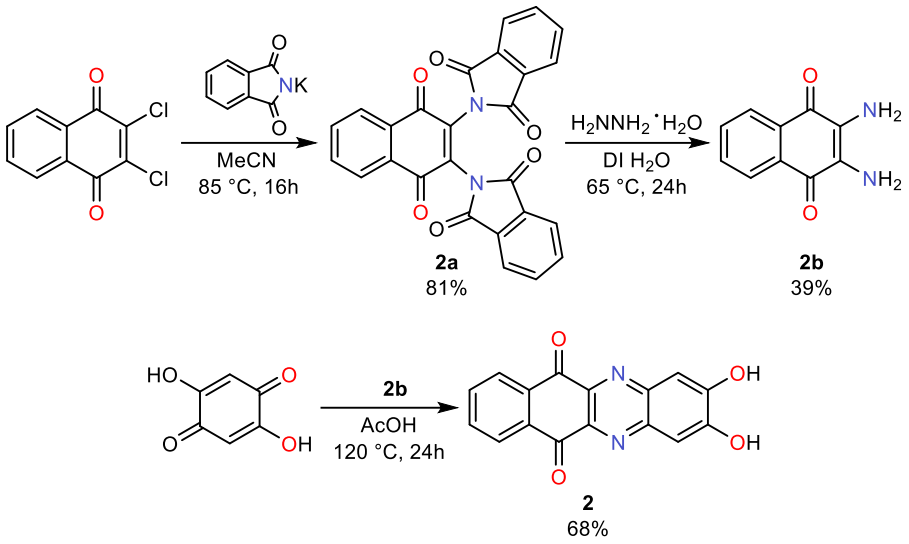


**Synthesis and characterization of 2,3-diphthalimido-1,4-naphthoquinone (2a)**

2,3-Diphthalimido-1,4-naphthoquinone was prepared according to a modified literature procedure.[3,4] In a roundbottom flask, a mixture of dichloronapthoquinone (1.00 g, 4.40 mmol) and potassium phthalimide (1.71 g, 9.25 mmol) in MeCN (50 mL) was refluxed at 85 °C overnight, resulting in a dark brown reaction mixture with yellow precipitate. After cooling to room temperature, the precipitate was filtered, washed the with DI water until the filtrate was clear, and dried *in vacuo* at 90 ºC overnight to yield the product as a dark yellow solid (1.59 g, 81% yield). $^1$H NMR (DMSO-$d_6$, 400 MHz): δ 8.20 (m, 2H), δ 8.07 (m, 2H), δ 7.98 (m, 4H), δ 7.95 (m, 4H) (Figure S2).

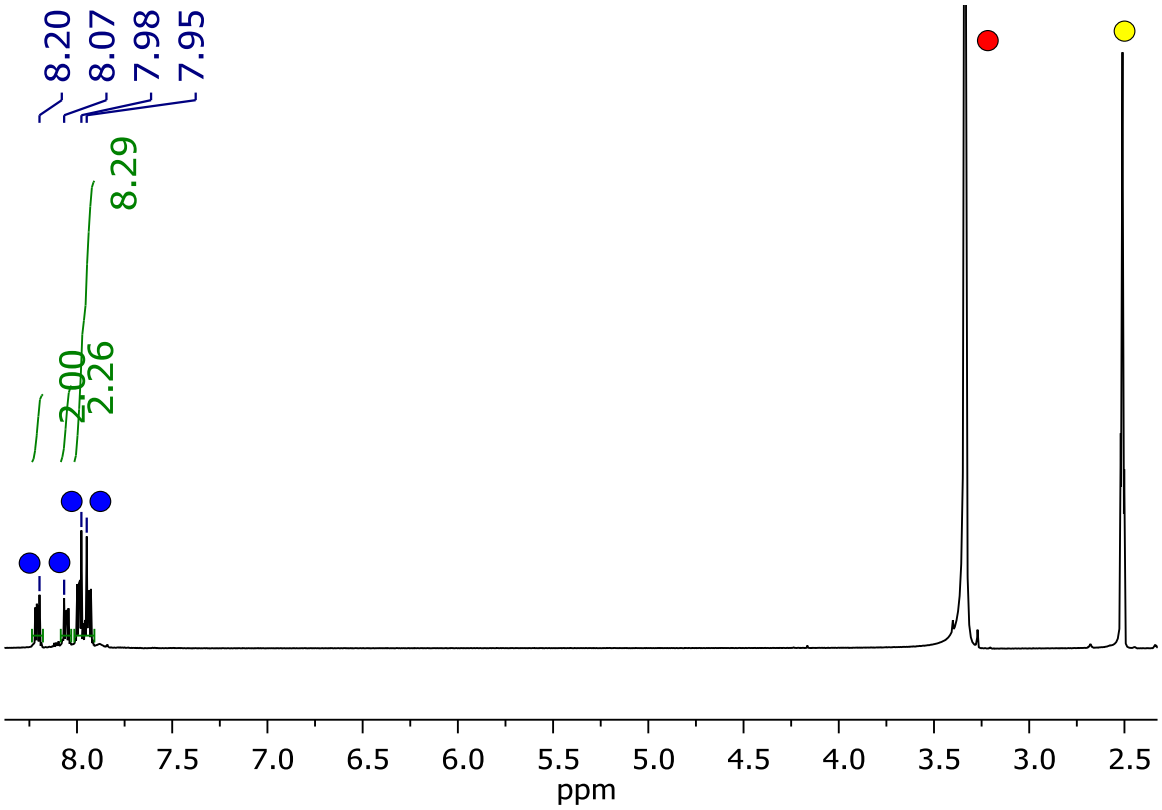


**Figure S2.** $^{1}$H NMR (DMSO-$d_6$, 400 MHz) spectrum of 2,3-diphthalimido-1,4-naphthoquinone (**2a**). Blue dots indicate product; yellow dot indicates NMR solvent (δ 2.51 - DMSO-$d_6$); and red dot indicates solvent impurity (δ 3.33 – $H_2O$).

**Synthesis and characterization of 2,3-diamino-1,4-naphthoquinone (2b)**

2,3-Diamino-1,4-naphthoquinone was prepared according to a modified literature procedure.[3,4] To a suspension of 2,3-diphthalimido-1,4-naphthoquinone (**2a**, 2.92 g, 6.51 mmol) in DI water (200 mL) was added hydrazine hydrate (64% in water, 27 mL, 0.796 mol). The solution was stirred for 15 minutes at room temperature and then heated to 65º C for 24 hours. After cooling to room temperature, the precipitate collected by filtration, washed with water until the filtrate was clear, and dried at 105 °C overnight to yield the product as a dark purple solid (0.450 g, 39%). $^{1}$H NMR (DMSO-$d_6$, 400 MHz): δ 7.75 (m, 2H), δ 7.61 (m, 2H), δ 5.45 (s, 4H). The $^{1}$H NMR spectrum of the product matches that reported in the literature.[4]

**Synthesis and characterization of 2,3-dihydroxybenzo[b]phenazine-6,11-dione (2)**

In a roundbottom flask, a mixture of 2,5-dihydroxy-1,4-benzoquinone (0.148 g, 1.06 mmol) and 2,3-diamino-1,4-naphthoquinone (**2b**, 0.200 g, 1.06 mmol) in glacial AcOH (5 mL) was heated at 120 °C for 24 hours. After cooling to room temperature, the the precipitate was collected by filtration, washed with DI water and acetone until the filtrate was clear, and dried at 105 °C overnight to yield the product as a dark yellow-green solid (0.210 g, 68%). mp: decomposition observed around 408 °C (Figure S5). $^{1}$H NMR (DMSO-$d_6$, 400 MHz): δ 11.42 (br s, 2H), δ 8.26 (dd, $J_1$=5.73 Hz, $J_2$=3.31 Hz, 2H), δ 7.95 (dd, $J_1$=6.00 Hz, $J_2$=3.29 Hz, 2H), δ 7.47 (s, 2H). $^{13}$C NMR (DMSO-$d_6$, 100 MHz): δ 181.7, δ 155.4, δ 142.5, δ 141.4, δ 135.0, δ 134.2, δ 127.4, δ 110.3. IR (ATR, cm-1): 3260, 1673, 1586, 1582, 1527, 1518, 1456, 1386, 1346, 1253, 1208, 1188, 1159, 1115, 1037, 987, 918, 877, 800, 720, 666, 534, 482, 460, 457, 427 (Figure S3). HRMS-ESI (*m/z*) calcd for $C_{16}H_7N_2O_4$ ($[M–H]^-$ ): 291.0411, found: 291.0411.

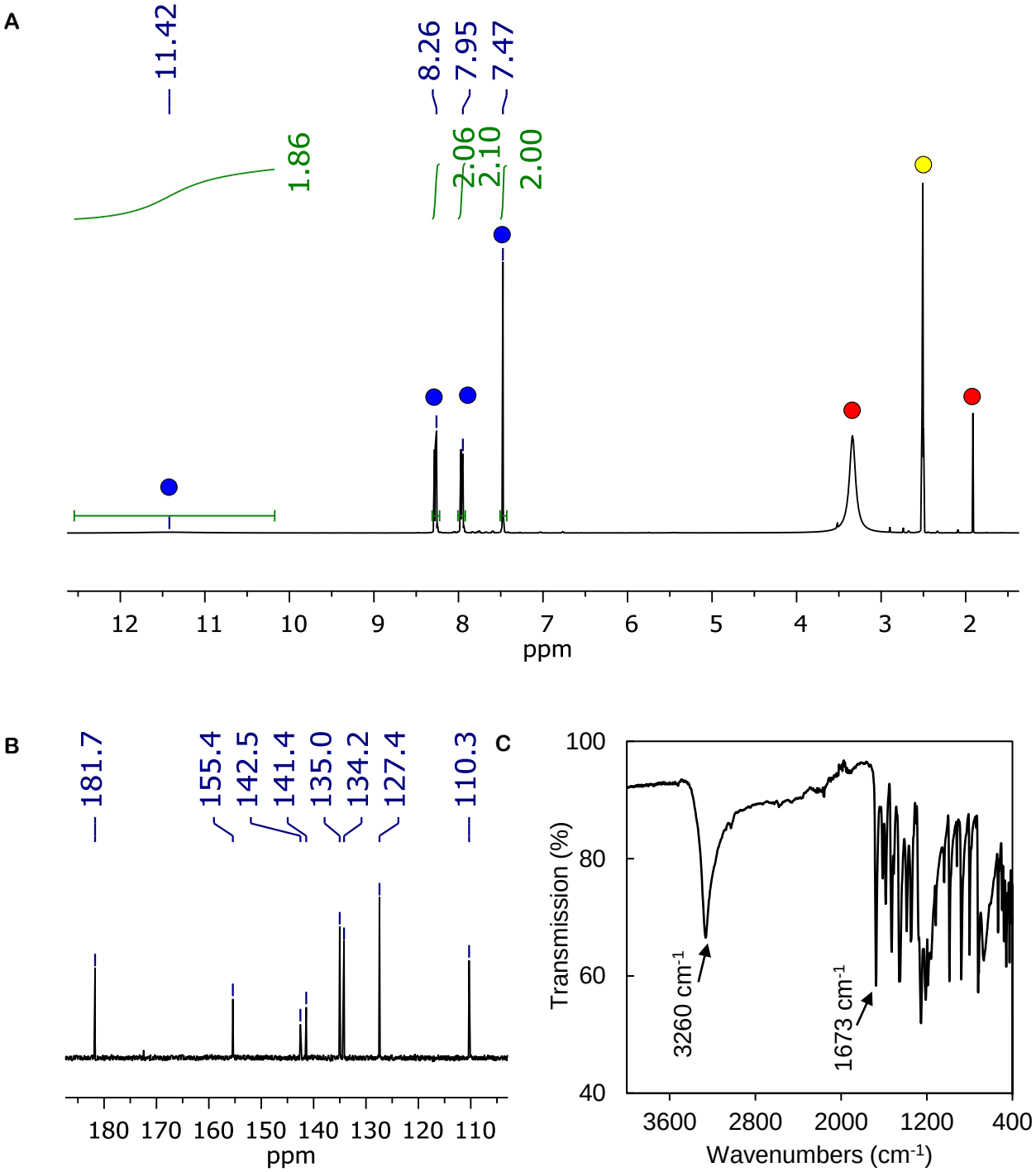


**Figure S3.** (A) $^{1}$H NMR (DMSO-$d_6$, 400 MHz), (B) $^{13}$C NMR (DMSO-$d_6$, 100 MHz), and (C) IR (ATR, cm$^{-1}$) spectra of 2,3-dihydroxybenzo[b]phenazine-6,11-dione (**2**). Blue dots indicate product; yellow dot indicates NMR solvent (δ 2.51 - DMSO-$d_6$); and red dots indicate solvent impurities (δ 3.33 – $H_2O$, δ 1.91 – AcOH).

**Scheme S3.** Synthesis of **QAP 3**

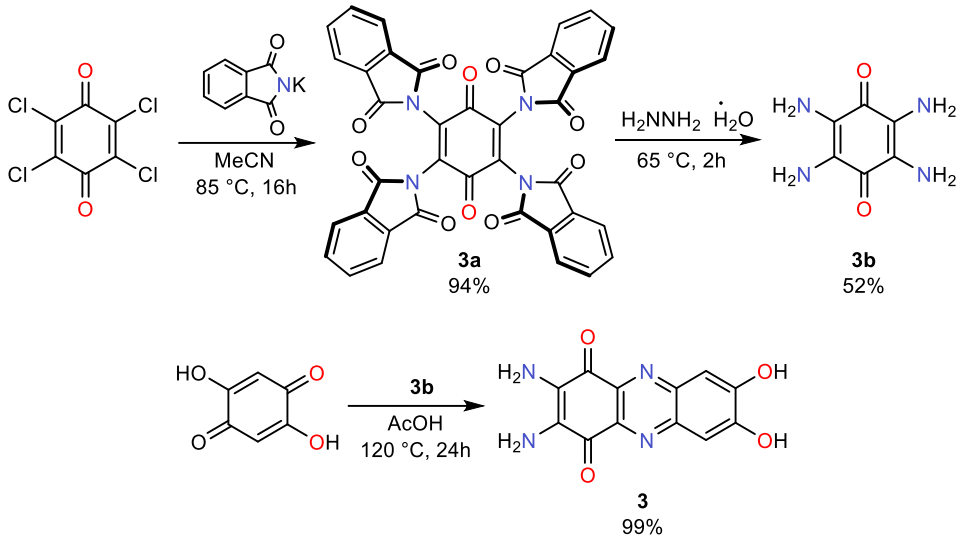


**Synthesis and characterization of 2,3,5,6-tetraphthalimido-1,4-benzoquinone (3a)**

2,3,5,6-tetraphthalimido-1,4-benzoquinone was prepared according to a modified literature procedure.[5,6] In a pressure flask under an inert atmosphere, potassium phthalimide (6.63 g, 35.8 mmol) was added to a solution of *p*-chloranil (2.20 g, 8.95 mmol) in anhydrous MeCN (100 mL) and refluxed at 85 °C overnight. The reaction mixture was hot filtered, and the green-brown precipitate was washed with DMF (50 mL) and water (50 mL), and dried in a 105 °C oven overnight to yield the product as a dark yellow solid (5.80 g, 94%). $^1$H NMR (DMSO-$d_6$, 400 MHz): δ 8.00 (s, 8H), δ 7.95 (s, 8H). The $^1$H NMR spectrum of the product matches that reported in the literature.[5]

**Synthesis and characterization of 2,3,5,6-tetraamino-1,4-benzoquinone (3b)**

2,3,5,6-tetraamino-1,4-benzoquinone was prepared according to a modified literature procedure.[5,6] In a roundbottom flask, a mixture of 2,3,5,6-tetraphthalimido-1,4-benzoquinone (**3a**, 1.25 g, 1.82 mmol) and hydrazine hydrate (64% in water, 15 mL, 0.198 mol) was heated at 65 °C for 2 hours, gradually turning black. After cooling to room temperature, the reaction mixture was filtered, and the resulting black precipitate was washed with water (100 mL) and THF (100 mL) and dried in a 105 °C oven overnight (0.421 g, 52%). $^1$H NMR (DMSO-$d_6$, 400 MHz): δ 4.55 (s, 8H). The $^1$H NMR spectrum of the product matches that reported in the literature.[6]

**Synthesis and characterization of 2,3-diamino-7,8-dihydroxyphenazine-1,4-dione (3)**

In a roundbottom flask, a mixture of 2,5-dihydroxy-1,4-benzoquinone (0.200 g, 1.43 mmol) tetraaminobenzoquinone (240 mg, 1.43 mM) and 2,3,5,6-tetraamino-1,4-benzoquinone (**3b**, 0.240 g, 1.43 mmol) in glacial AcOH (5 mL) was refluxed at 120 °C for 24 hr. After cooling to room temperature, the black reaction mixture was filtered, washed with water, MeOH, and acetone until the filtrate was clear, and dried *in vacuo* at 90 °C overnight to yield the product as a black powder (0.383 g, 99%). mp: decomposition observed around 377 °C (Figure S5). $^{1}$H NMR (DMSO-$d_6$, 400 MHz): δ 10.89 (br s, 2H), δ 7.32 (s, 2H), δ 5.91 (s, 4H). $^{13}$C NMR (DMSO-$d_6$, 400 MHz): δ 176.1, δ 153.1, δ 142.1, δ 139.5, δ 130.8, δ 111.0. IR (ATR, cm$^{-1}$): 3470, 3441, 3338, 3298, 3119, 1628, 1560, 1553, 1523, 1497, 1451, 1413, 1386, 1334, 1255, 1149, 877, 846, 814, 731, 654, 652, 563, 500, 476 (Figure S4). HRMS-ESI (*m/z*) calcd for $C_{12}H_7N_4O_4$ ([M–H]$^-$ ): 271.0473, found: 271.0468.

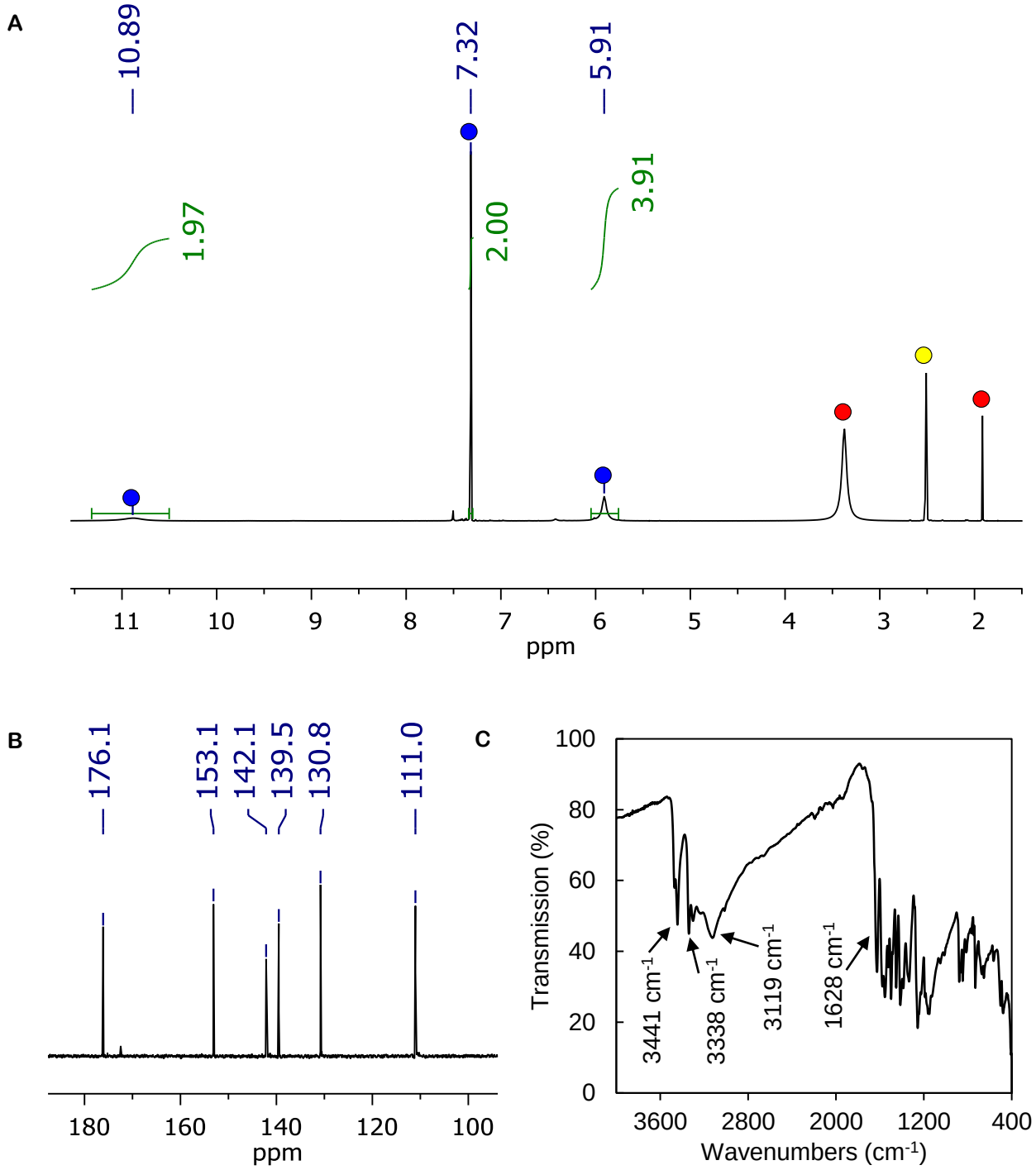


**Figure S4.** (A) $^{1}$H NMR (DMSO-$d_6$, 400 MHz), (B) $^{13}$C NMR (DMSO-$d_6$, 100 MHz), and (C) IR (ATR, cm$^{-1}$) spectra of 2,3-diamino-7,8-dihydroxyphenazine-1,4-dione (**3**). Blue dots indicate product; yellow dot indicates NMR solvent (δ 2.51 - DMSO-$d_6$); and red dots indicate solvent impurities (δ 3.33 – $H_2O$, δ 1.91 – AcOH).

**Thermogravimetric Analysis and Differential Scanning Calorimetry**

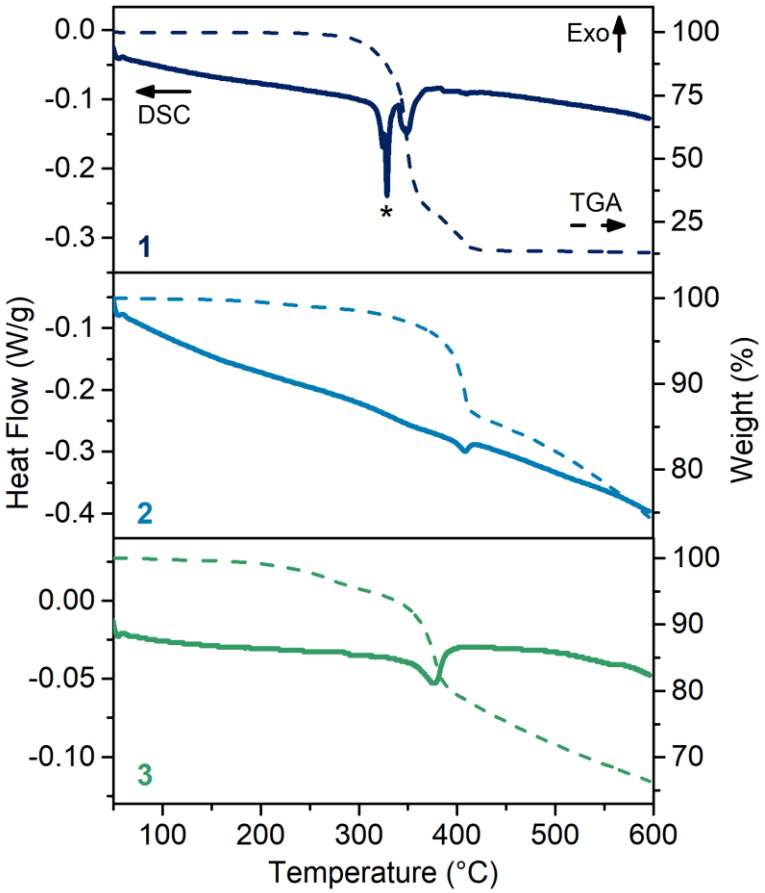


**Figure S5.** TGA-DSC results for compounds **1**-**3**. The asterisk marks the melting point of **1**.

**PXRD Measurements**

High-resolution synchrotron powder diffraction data of **2** and **3** were collected at the 11-BM beamline at the Advanced Photon Source with a wavelength of 0.4579 Å, step size 0.001°. Single crystal diffraction data of **1** has been previously published[2] and is available on the Cambridge Crystallographic Data Centre website (CCDC: 761662). We were unable the determine the structure of **2** due to the poor crystallinity of the sample.

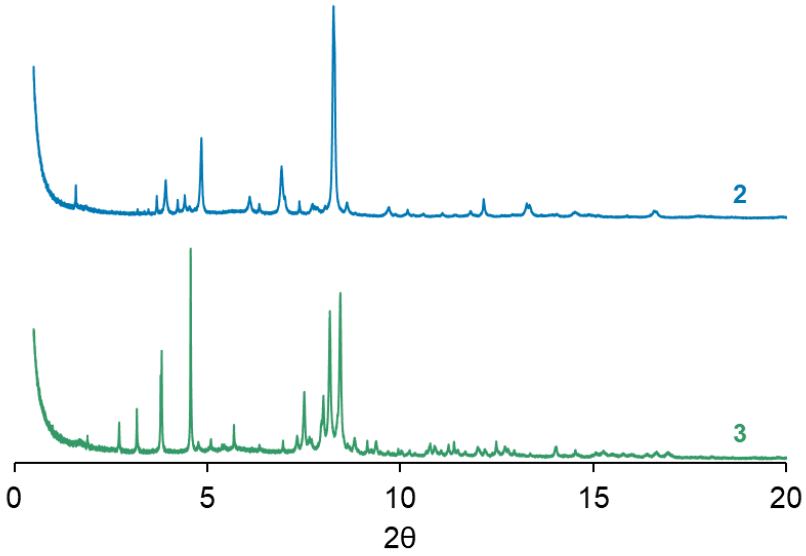


**Figure S6.** X-ray powder diffraction data of **2** (top) and **3** (bottom) collected at the APS 11-BM beamline.

**Rietveld Refinement of 3**

Powder pattern indexing, unit cell determination, Pawley refinement, and Reitveld refinement of **3** were completed using GSAS-II software.[7]

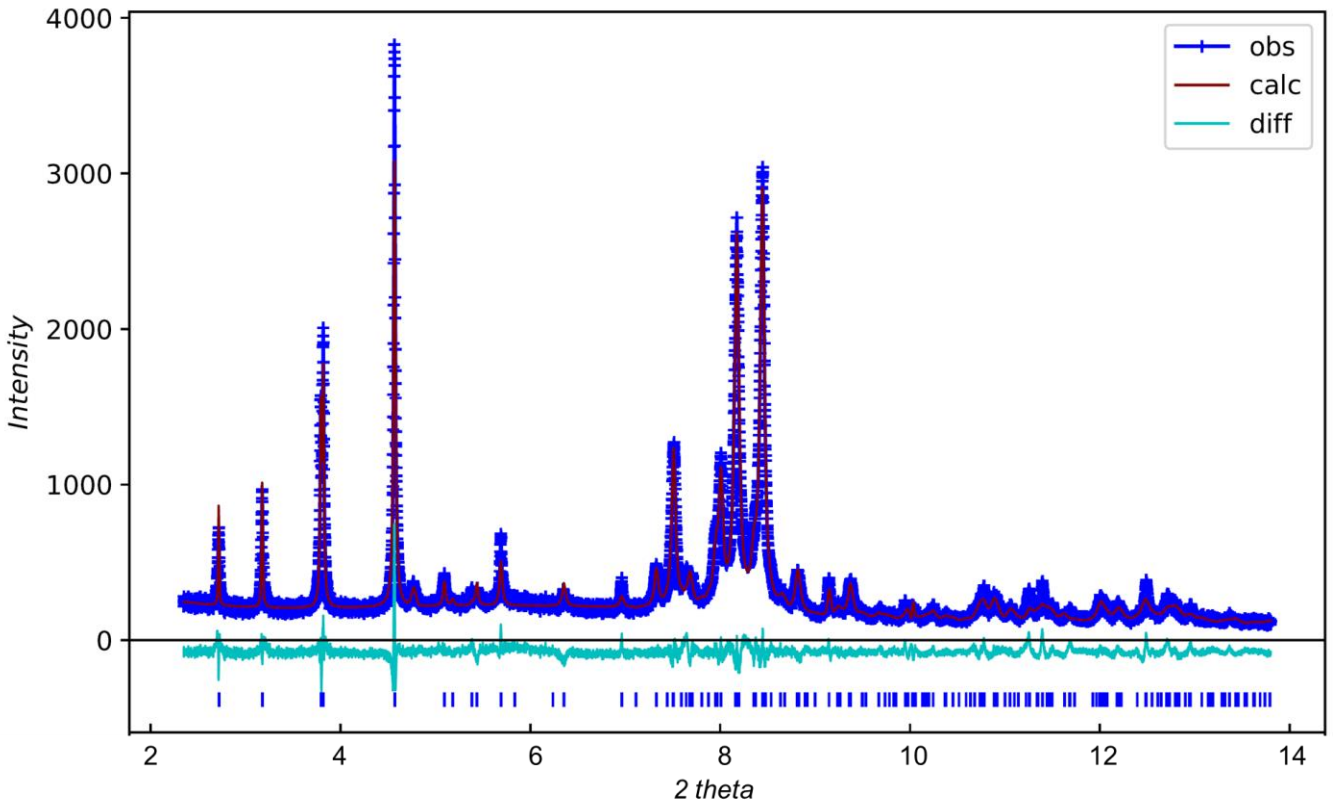


**Figure S7.** X-ray powder diffraction pattern (dark blue, observed intensity) and final Rietveld refinement (red, calculated intensity) of **3**. The residual difference between the calculated and experimental pattern is shown in light blue. The *hkl* reflection positions were indicated by blue ticks.

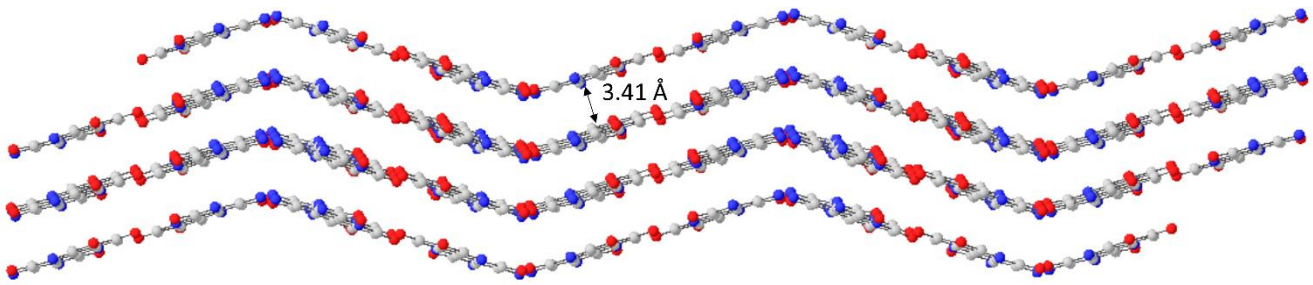


**Figure S8.** Illustration of parallel layers of **3** with π-π stacking interactions.

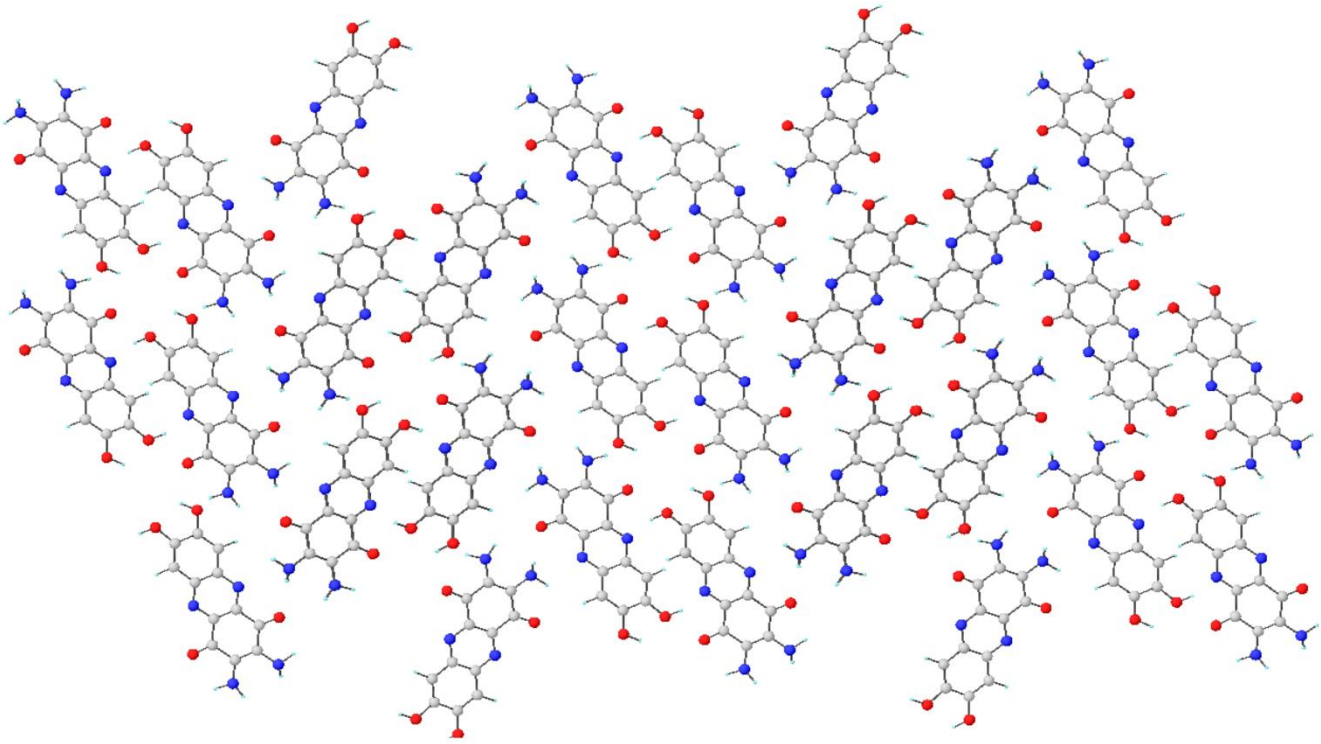

**Figure S9.** Illustration of parallel layers of **3** with hydrogen-bonding interactions.

**Table S1**. Data collection and structure refinement parameters for **3**.

| Unit cell | | Data collection | | Refinement | |
|---|---|---|---|---|---|
| *Space group* | $P2_1/n$ | $\lambda$ (Å) | 0.4579 | $R_{wp}$ | 0.093 |
| *a* (Å) | 11.860 | Temperature | 100 K | $R_{(F)}$ | 0.051 |
| *b* (Å) | 27.669 | θmin−θmax (deg.) | 2 - 50 | | |
| *c* (Å) | 3.5753 | 2θ step | 0.001 | | |
| $\beta$ (deg) | 119.64 | | | | |
| *V* (Å$^3$) | 1019.8 | | | | |
| *Z* | 4 | | | | |

**Table S2**. Crystallographic coordinates of **3** after final Rietveld refinement.

| | | | |
|---|---|---|---|
| H | 0.314110179 | 0.660169881 | 0.487599956 |
| C | 0.888169745 | 0.696289874 | 0.143289987 |
| C | 0.755819861 | 0.701739873 | 0.248199978 |
| C | 0.934129659 | 0.653009882 | 0.031709997 |
| O | 0.718609935 | 0.741089866 | 0.345479969 |
| N | 1.057779549 | 0.647929883 | -0.068869994 |
| C | 0.670329879 | 0.658009881 | 0.224199980 |
| C | 0.852979670 | 0.609349890 | -0.001900000 |
| O | 0.897989591 | 0.571409897 | -0.101969991 |
| C | 0.716699783 | 0.613399889 | 0.096099991 |
| N | 0.964279737 | 0.737139867 | 0.176589984 |
| H | 0.913109786 | 0.767139861 | 0.225639980 |
| H | 1.027159595 | 0.741519866 | -0.014409999 |
| H | 1.081569515 | 0.613039889 | -0.109079990 |
| H | 1.127879612 | 0.667359879 | 0.077079993 |
| N | 0.552139984 | 0.662749880 | 0.319909971 |
| C | 0.475369995 | 0.623219887 | 0.290439974 |
| N | 0.643689791 | 0.574459896 | 0.064009994 |
| C | 0.347510105 | 0.625979887 | 0.389009965 |
| C | 0.521719897 | 0.578439895 | 0.159609986 |
| C | 0.438589912 | 0.537939903 | 0.131379988 |
| O | 0.229260040 | 0.504149909 | 0.209169981 |
| C | 0.314690019 | 0.541379902 | 0.228439980 |
| O | 0.144580221 | 0.586019894 | 0.448949960 |
| H | 0.258769977 | 0.473579914 | 0.125609989 |
| C | 0.268310118 | 0.586209894 | 0.359679968 |
| H | 0.475289836 | 0.504339909 | 0.031819997 |
| H | 0.107210239 | 0.554409900 | 0.455919959 |

## Electrochemical Measurements

### Solution Phase Cyclic Voltammetry

Solution phase cyclic voltammetry (CV) experiments were carried out using a three-electrode cell, consisting of a glassy carbon working electrode (0.07 $cm^2$, CH Instruments), a $Ag^+/Ag$ reference electrode (CH Instruments) with 0.01 M $AgNO_3$ in MeCN, and a platinum wire counter electrode (7.5 cm, BASi). Solution CV experiments were performed at 1 mM concentrations under an atmosphere of $N_2$ with degassed electrolyte solutions of 0.1 M $LiClO_4$ in DMSO at variable concentrations and scan rates.

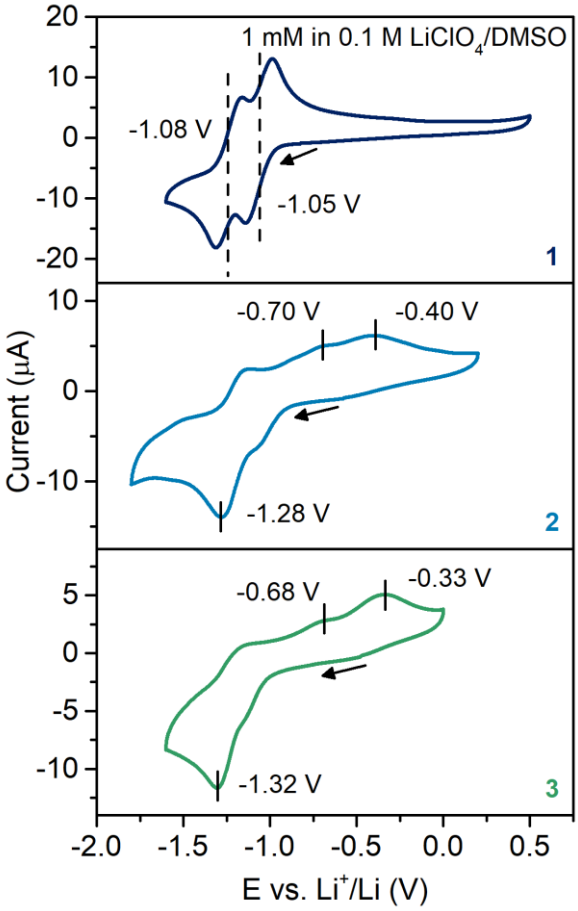


**Figure S10.** Solution CV data of **1**-**3** (1 mM) in 0.1 M $LiClO_4$/DMSO. Scan direction is marked with arrows. Redox couples and reduction/oxidation peaks are labeled.

The lack of two distint redox couples and the large separation between the reduction and oxidation peaks (Figure S10) suggest that **2** and **3** may exhibit redox-responsive proton transfer from the catechol moiety to the quinone moiety due to strong intermolecular HB in solution.[8] As the quinone (Q) moiety is reduced to $Q^{\bullet-}$, intermolecular proton transfer from the catechol moiety (-OH) can occur to generate the protonated radical species $HQ^{\bullet}$. Since $HQ^{\bullet}$ is easier to reduce than Q, $HQ^{\bullet}$ undergoes immediate irreversible reduction to $HQ^{-}$, resulting in doubling of the reduction peak current. The subsequent irreversible oxidation peaks describe the two-electron oxidation of $HQ^{-}$ back to Q.

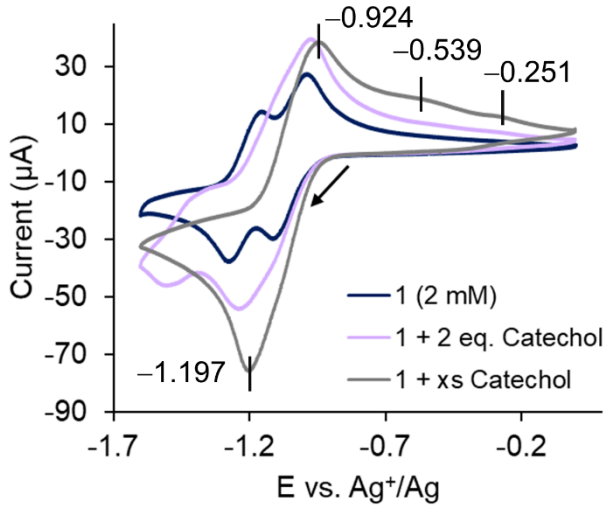


**Figure S11.** Solution CV of **1** in the presence of 0 eq. catechol (dark blue), 2 eq. catechol (purple), and excess catechol (gray). Scan direction is marked with an arrow.

Scan rate-dependent solution CV experiments were performed with IR compensation to obtain a plot of potential vs. log of scan rate (Figure S11) and determine the number of electrons involved in each electrochemical process. The slope of this plot is equal to the Laviron equation,

$$\frac{2.3RT}{\alpha Fn}$$

where R is the ideal gas constant (8.314 J $K^{-1}$ $mol^{-1}$), T is temperature (298 K), α is the electron transfer coefficient and assumed to be 0.5 for an irreversible process,[9] F is Faraday's constant (96485 C $mol^{-1}$), and n is the number of electrons involved in the electrochemical process. $n_c$, the number of electrons involved in the cathodic process, was calculated to be 2.0 for **2** and 2.2 for **3** (Figure S11). $n_a$, the number of electrons involved in the anodic process, was calculated to be 2.1 for both **2** and **3** (Figure S11). These results suggest that both the reduction and oxidation of **2** and **3** are two-electron processes. We also considered the possibility of a redox-responsive dimerization mechanism similar to the hydrogen-bonded ferrocene dimers studied by Smith and coworkers,[10] however, our experiments with **1** in the presence of catechol and the lack of changes in peak shape of **1-3** with scan rate suggests a proton transfer-

based ECE mechanism is more likely.

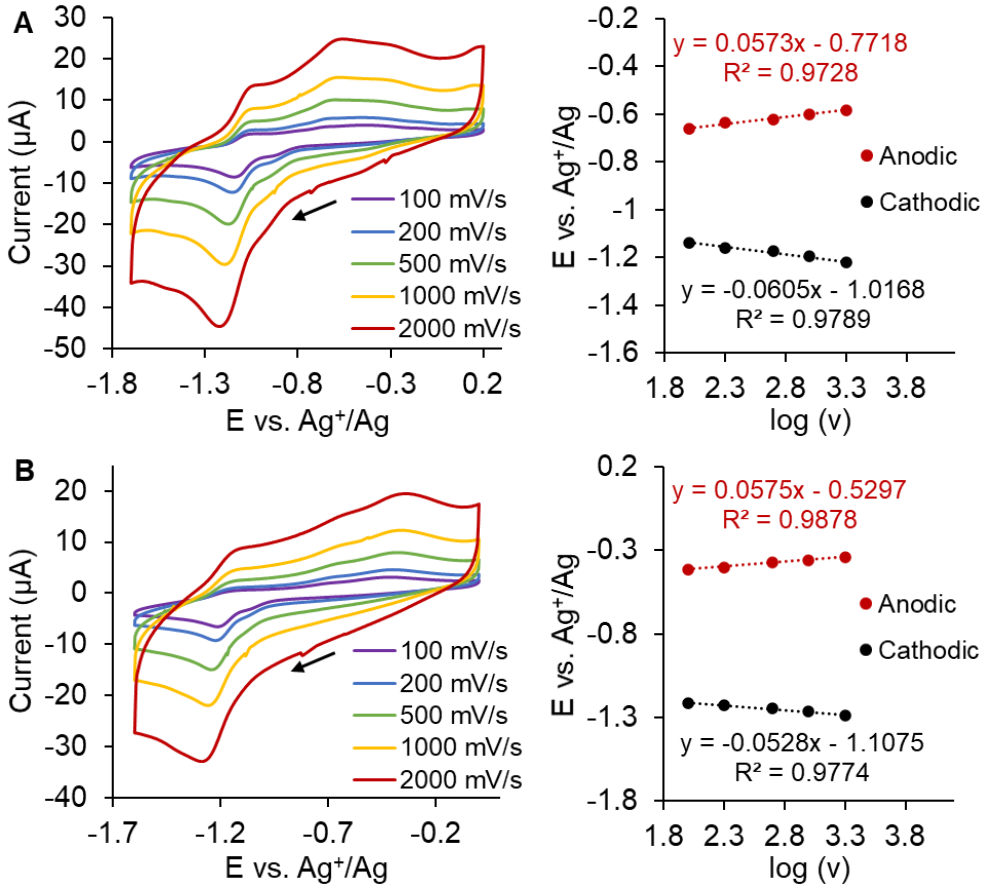


C

| | 2 | 3 |
|---|---|---|
| $n_a$ | 2.1 | 2.1 |
| $n_c$ | 2.0 | 2.2 |

**Figure S12.** Scan rate-dependent CV data for (A) **2** and (B) **3** (0.7 mM) in 0.1 M $LiClO_4$/DMSO. (C) The corresponding number of electrons involved in each electrochemical process calculated from the Laviron equation (above). Scan direction is marked with arrows.

**Solid State Cyclic Voltammetry**

Solid-state CV experiments were carried out using a two-electrode coin-type cell, consisting of a cathode of **1-3** and an anode of Li metal (see Battery Testing). Solid-state CV experiments were performed at a scan rate of either 0.1 $mV^{-1}$ (Figure 3A), 1 mV $s^{-1}$ (Figure S13) after an initial rest period of one hour.

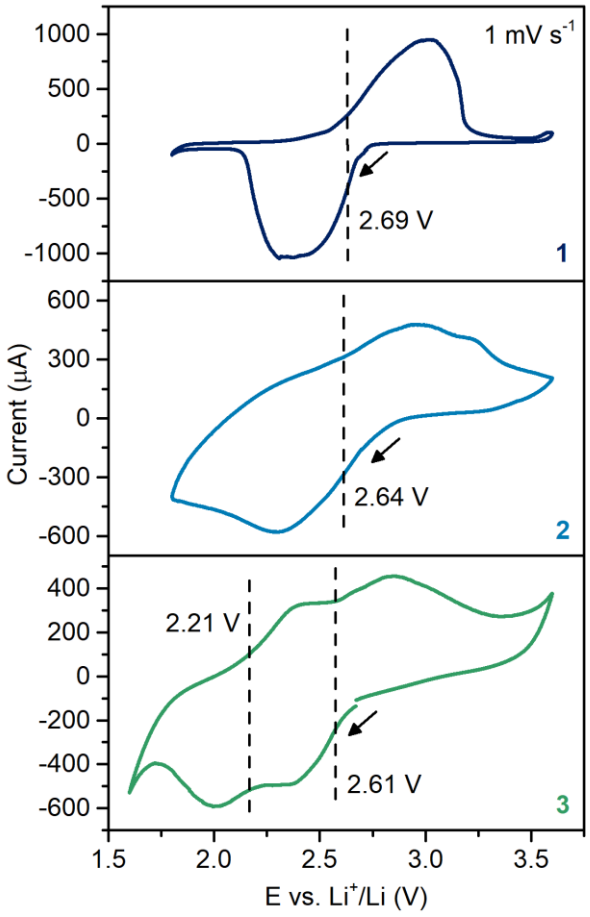


**Figure S13.** Solid-state CV data of **1-3** at a scan rate of 1 mV $s^{-1}$. Scan direction is marked with arrows. The redox potentials of each couple are labeled with dashed lines.

## Battery Testing

### Electrode Fabrication

Electrode dry mixtures were prepared by mixing powders of **1-3** with conductive carbon (SuperP) and polyvinylidene fluoride (PVDF) binder in a 50:40:10 weight ratio using a mortar and pestle. Electrode slurries were prepared by adding *N*-methylpyrrolidinone (NMP) to the dry mixture, vortexing for one minute, and sonicating for at least 30 minutes until a smooth ink was obtained. The inks were cast onto aluminum foil using the doctor-blade method (average mass loading density: *ca.* 1.7 mg $cm^{-2}$), dried in air overnight, and further dried in a vacuum oven at 80 °C overnight. After cutting the electrodes into 15 mm discs, they were dried again under vacuum at 90 °C for at least two hours and taken into an argon glovebox while still under vacuum.

### Coin Cell Assembly

Coin-type cells were assembled in an argon glovebox with **1-3** as the cathode, 1 M LiTFSI (lithium bis(trifluoromethanesulfonyl)imide) and 0.2 M $LiNO_3$ in 50:50 dimethoxyethane (DME) and dioxolane (DOL) as the electrolyte, Celgard as the separator, and Li metal as the anode. Coin cells were assembled bottom to top using materials purchased from Gelon: coin cell bottom, cathode disc, 40 μL electrolyte, separator, 40 μL electrolyte, Li anode, stainless steel current collector, wave/conical washer, coin cell top with gasket. Coin cells were crimped in a Gelon GN-CCM20 coin cell crimper at 900 psi and used for battery testing after a rest period of one hour.

### Galvanostatic Charge/Discharge Cycling

Coin-type cells with **1-3** cathodes were subjected to galvanostatic cycling using an automated testing system with lower voltage limits and upper voltage limits selected based on solid-state CV studies (*vide supra*). The currents for galvanostatic measurements were calculated based on the theoretical specific capacity of each compound. Priming periods for **1-3** consisted of 10 cycles at a rate of 0.5C.

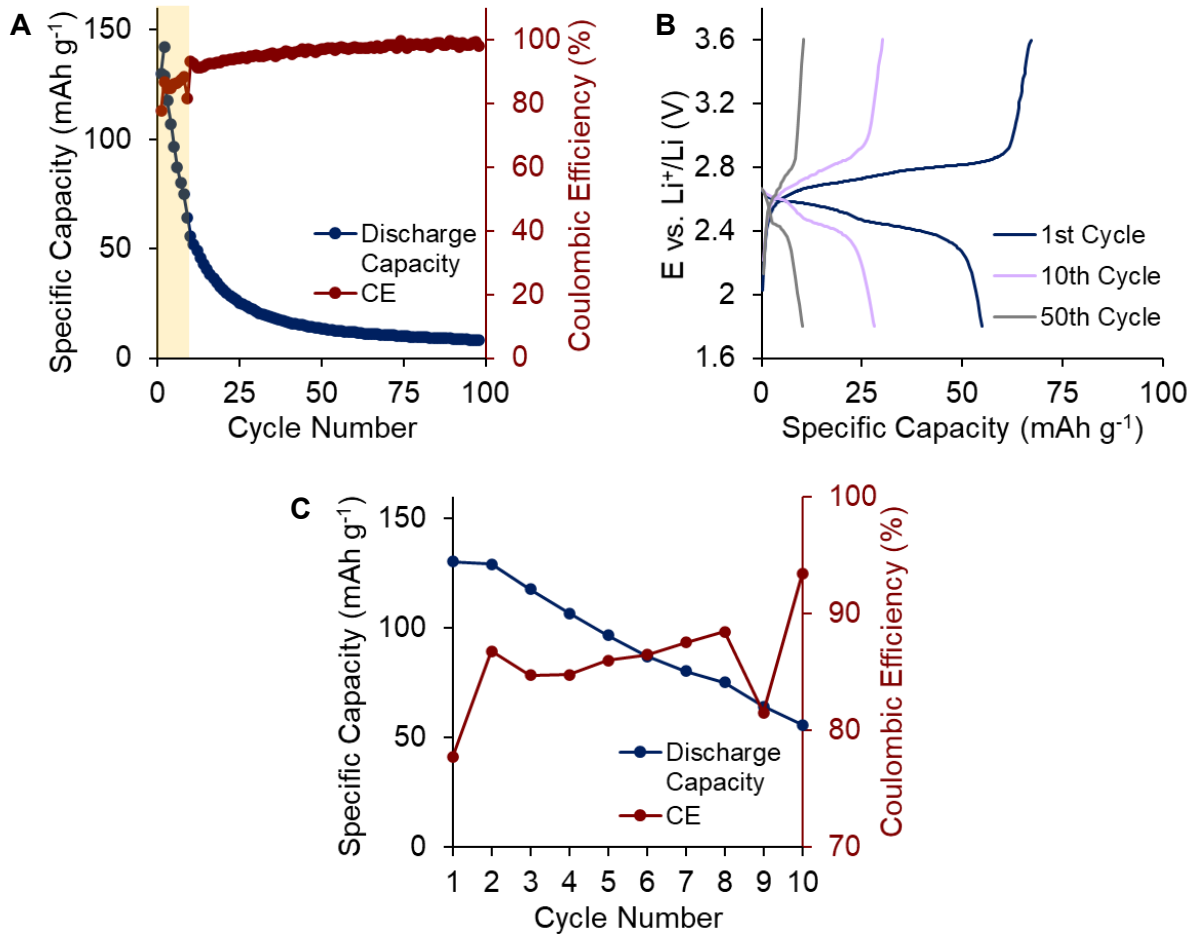


**Figure S14.** (A) Galvanostatic cycling data of **1** at a rate of 1C (206 mA $g^{-1}$) including the priming period, highlighted in yellow. (B) Charge-discharge curves of **1** at a rate of 1C. The legend refers to the cycle number after the priming period. (C) Cycling data of **1** during the priming period.

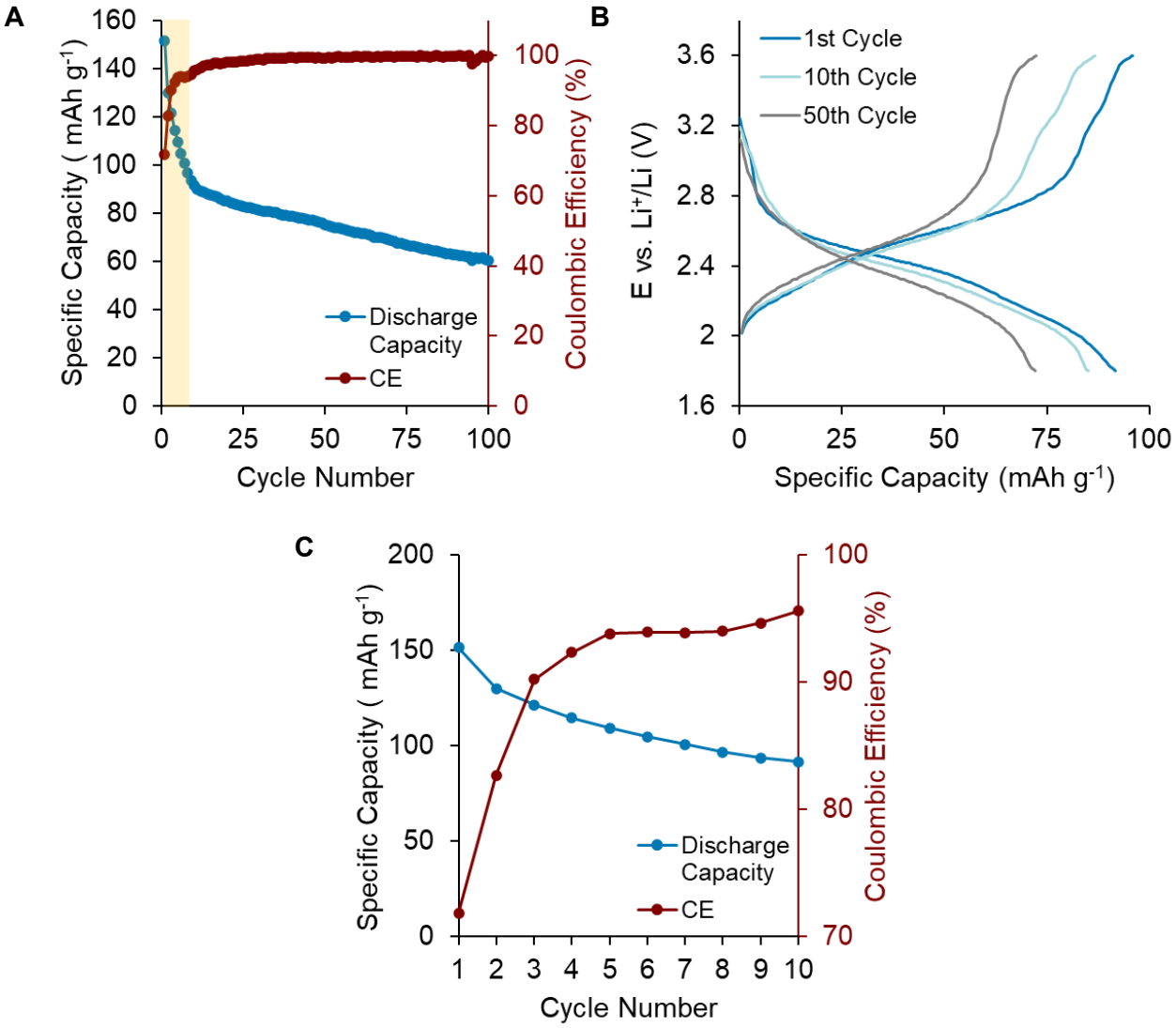


**Figure S15.** (A) Galvanostatic cycling data of **2** at a rate of 1C (183 mA $g^{-1}$) including the priming period, highlighted in yellow. (B) Charge-discharge curves of **2** at a rate of 1C. The legend refers to the cycle number after the priming period. (C) Cycling data of **2** during the priming period.

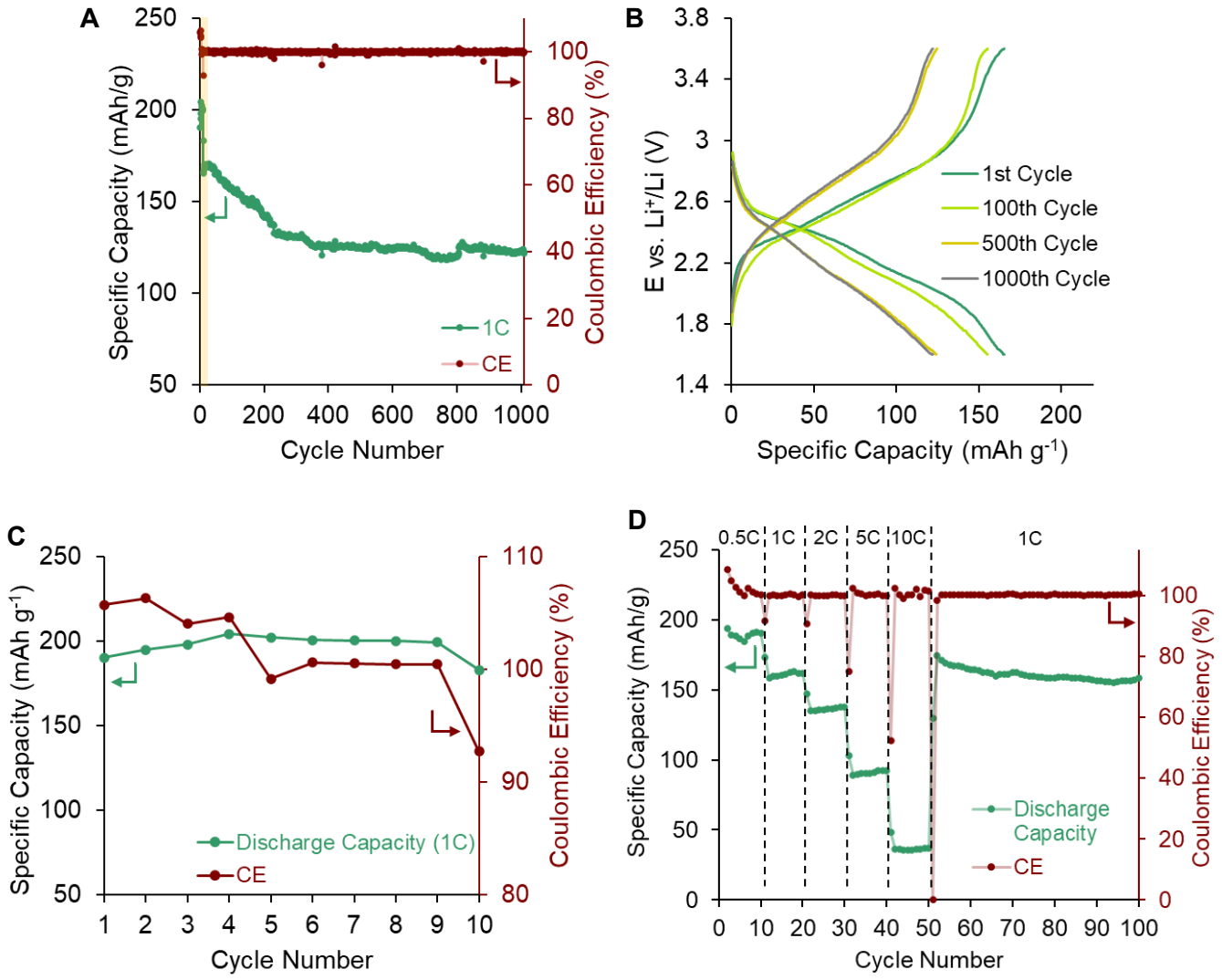


**Figure S16.** Galvanostatic cycling data of **3** at a rate of (A) 1C (197 mA $g^{-1}$) including the priming period, highlighted in yellow. (B) Charge-discharge curves of **3** at a rate of 1C. The legend refers to the cycle number after the priming period. (C) Cycling data of **3** during the priming period. (D) Rate-dependent cycling data of **3**.

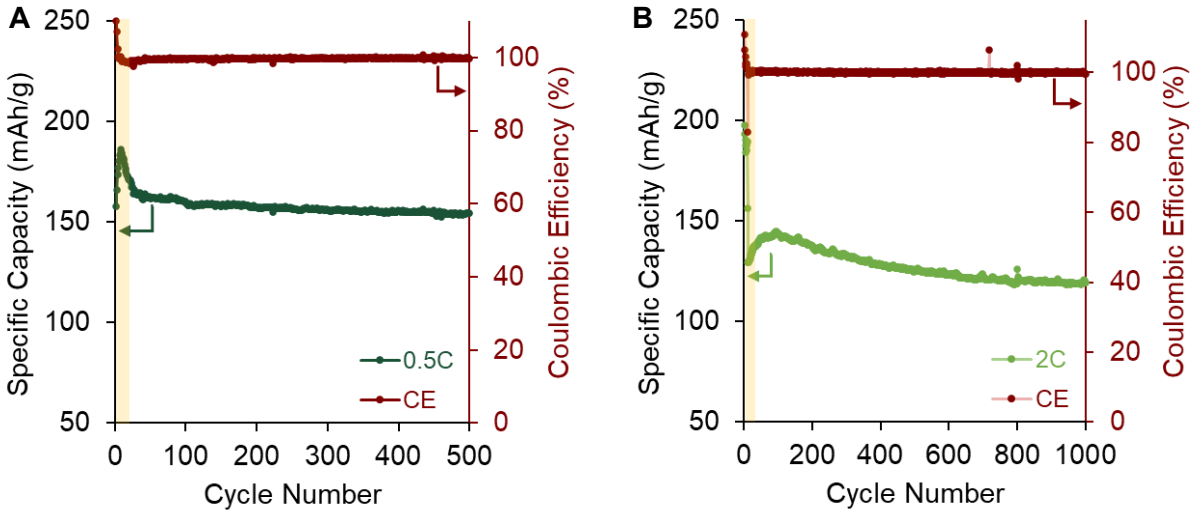


**Figure S17.** Galvanostatic cycling data of **3** at a rate of (A) 0.5C (98 mAh $g^{-1}$) and (B) 2C (394 mAh $g^{-1}$) including the priming periods, highlighted in yellow.

**Coin Cell Disassembly**

The battery was taken into an Ar glovebox after 24 hours of galvanostatic cycling, and disassembled on a Gelon GN-CCM20 coin cell crimping machine equipped with a disassembly die set. Pictures of the electrodes and separators were taken upon disassembly. To prepare the cathodes for ex-situ analysis, they were washed with DME (3 × 50 μL) and dried *in vacuo* for at least 30 minutes.

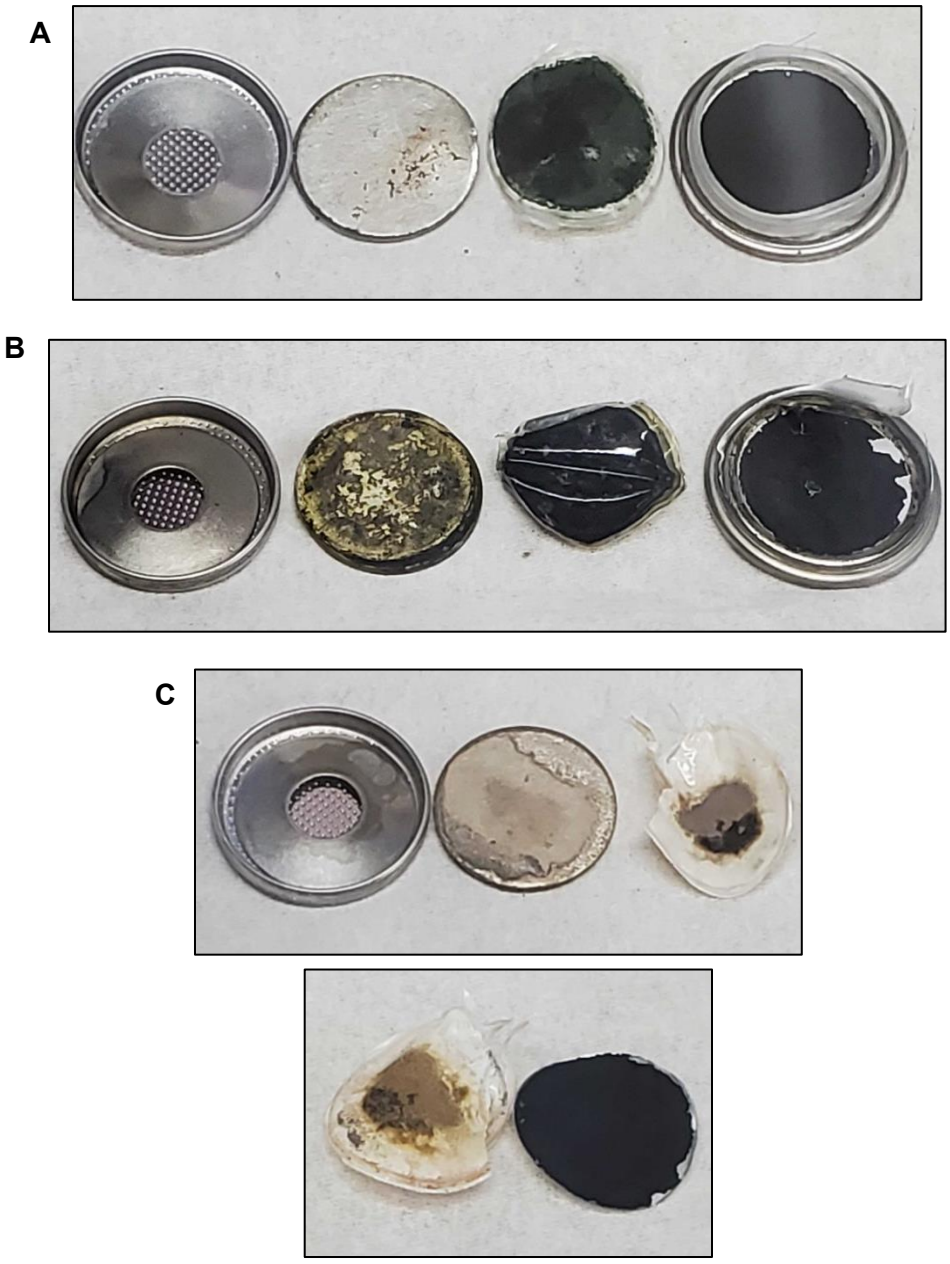


**Figure S18.** Digital pictures of disassembled coin cells of (A) **1** (from left to right: coin cell top, Li anode, Celgard separator, QAP cathode), (B) **2** (from left to right: coin cell top, Li anode, Celgard separator, QAP cathode), and (C) **3** (top: coin cell top, Li anode, Celgard separator (anode side); bottom: Celgard separator (cathode side), QAP cathode).

**NMR Experiments**

**1D $^{1}$H VT-NMR**

VT-NMR experiments were carried out on a 600 MHz instrument from 27 °C to 75 °C. A 5:4 mixture of DMSO-$d_6$:$C_6D_6$ was used to resolve the NMR signals in **1-3** as much as possible without sacrificing solubility. Concentrations and temperature of each sample are labeled.

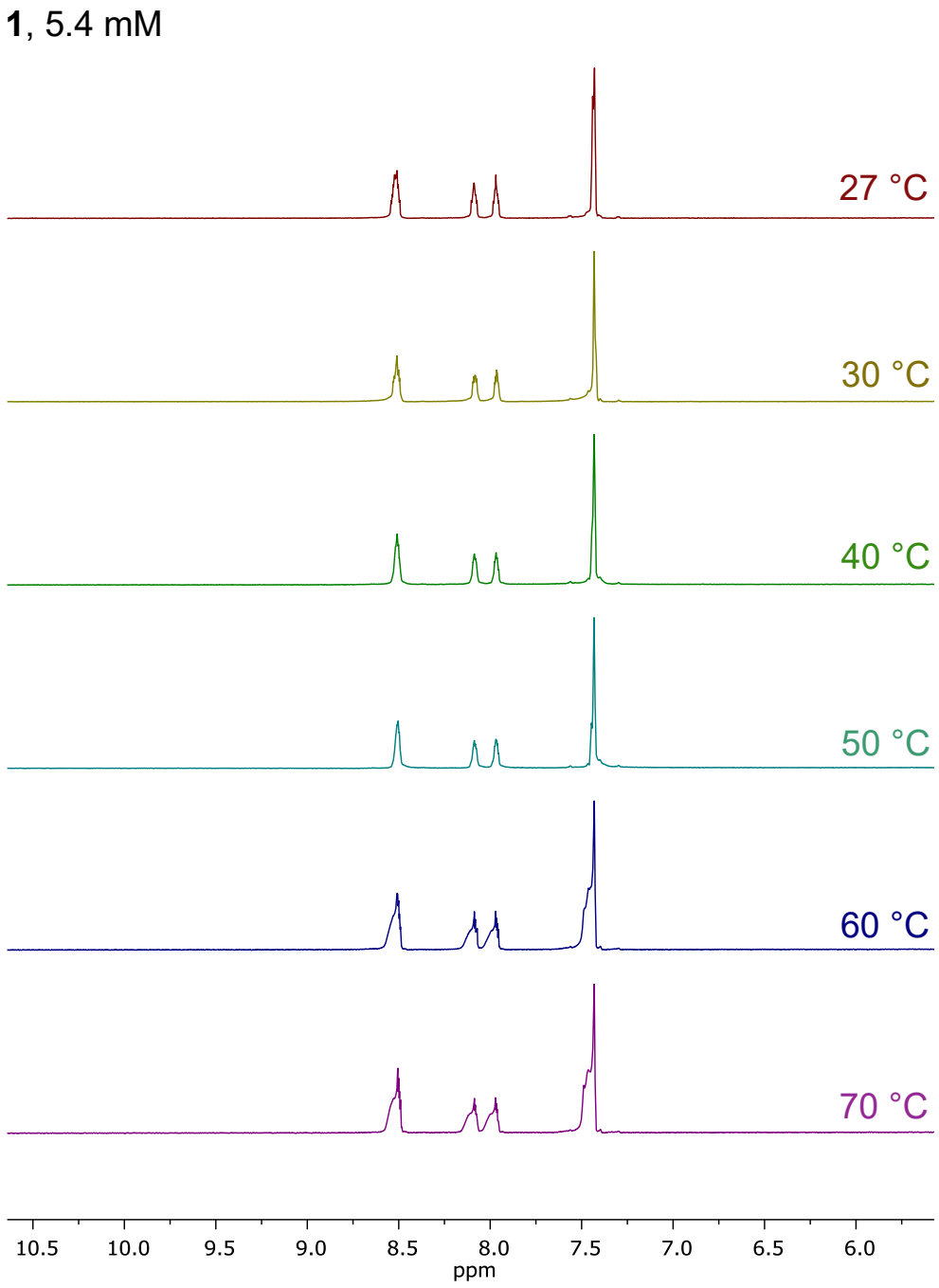


**Figure S19.** VT-NMR of the -CH peaks of **1.**

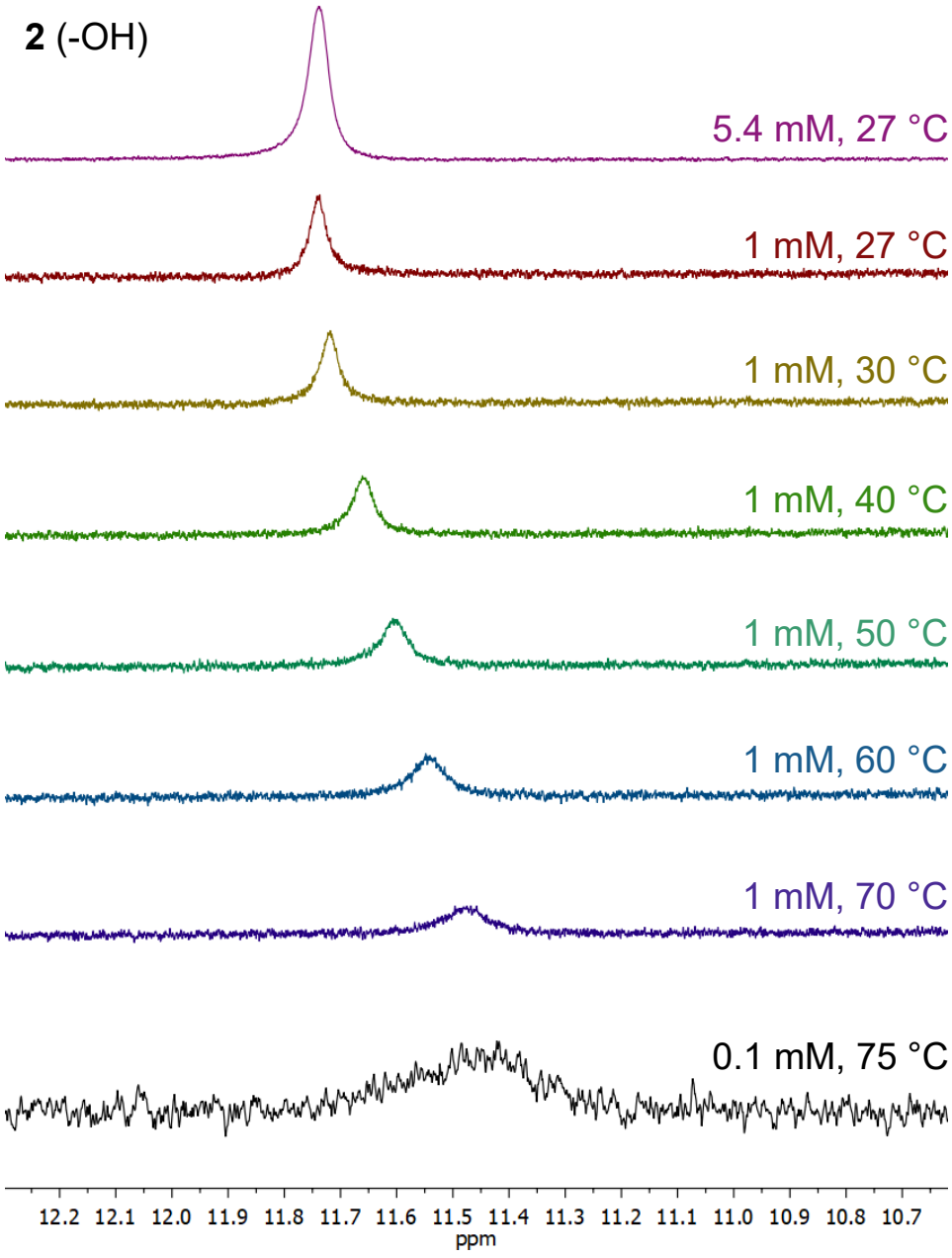


**Figure S20.** VT-NMR of the -OH peak of **2.** The chemical shift of -OH at 5.4 mM at 27 °C was used as the boundary limit $\delta_B$, and that of 0.1 mM at 75 °C was used as the boundary limit $\delta_N$.

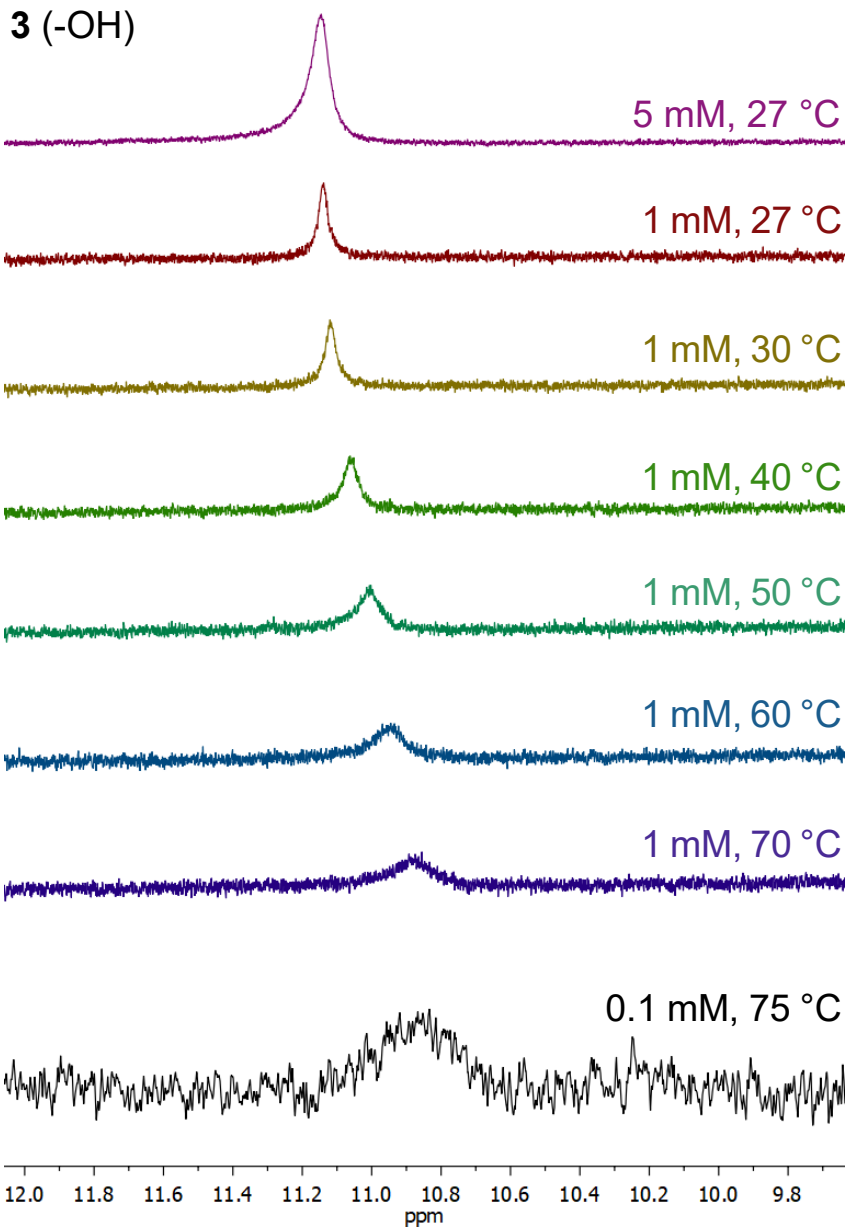


**Figure S21.** VT-NMR of the -OH peak of **3**. The chemical shift of -OH at 5 mM at 27 °C was used as the boundary limit $\delta_B$, and that of 0.1 mM at 75 °C was used as the boundary limit $\delta_N$.

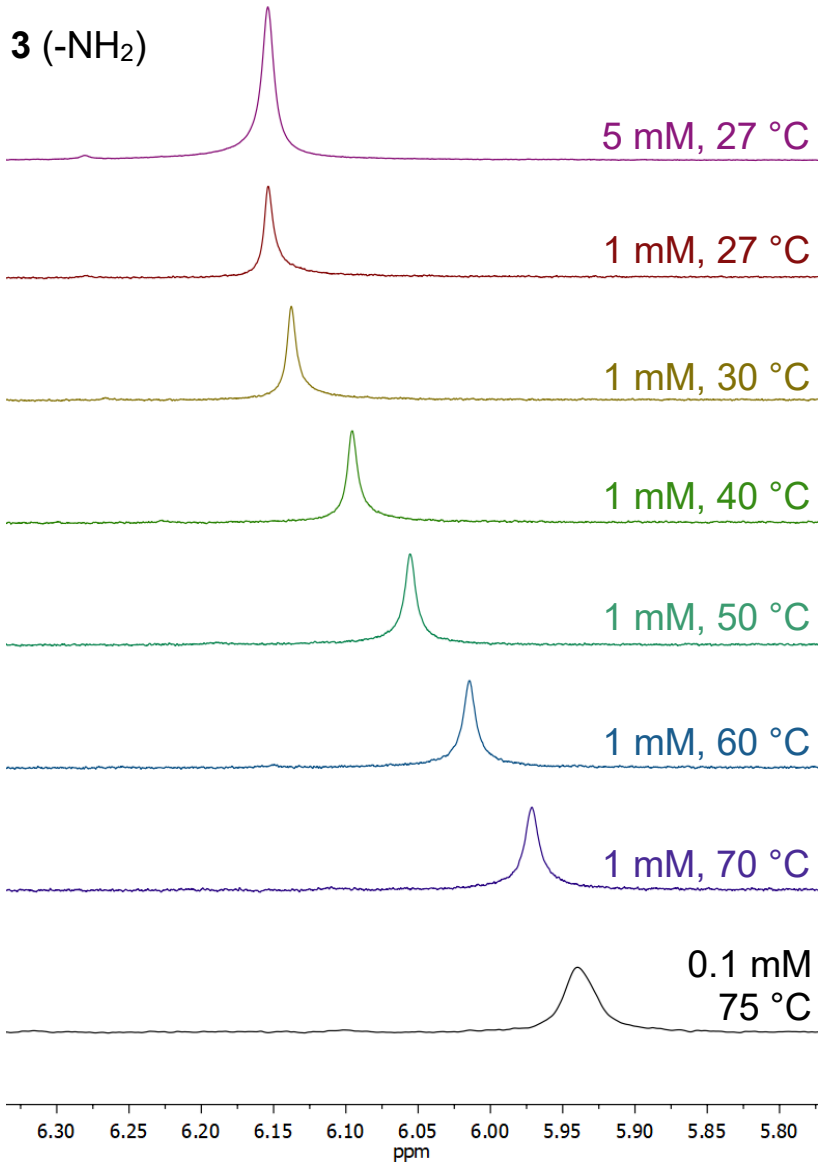


**Figure S22.** VT-NMR of the -$NH_2$ peak of **3**. The chemical shift of -$NH_2$ at 5 mM at 27 °C was used as the boundary limit $\delta_B$, and that at 0.1 mM at 75 °C was used as the boundary limit $\delta_N$.

The thermodyanamic parameters between hydrogen-bonded and a non-hydrogen-bonded states can be extracted by performing a van't Hoff analysis with $\delta$OH and $\delta$NH using the equation below:

$$K_{eq} = \frac{(\delta_{obs} - \delta_N)}{(\delta_B - \delta_{obs})}$$

where $\delta_{obs}$, $\delta_B$, and $\delta_N$ correspond to the observed chemical shift at each temperature, the chemical shift of hydrogen-bonded species, and the chemical shift of non-hydrogen-bonded species, respectively. Since intermolecular interactions are favored at high concentration and low temperature ($\Delta S° < 0$ for aggregation processes), the δOH and $\delta$NH values at 5 mM at room temperature (27 °C) were used as $\delta_B$, and those at 0.1 mM at 75 °C were used as $\delta_N$. These boundary chemical shifts were used to calculate $K_{eq}$ at different temperatures using the above equation, which then allowed construction of van't Hoff plots (Figures S20-21) using the equation below:

$$lnK_{eq} = \frac{\Delta S}{\mathrm{R}} - \frac{\Delta H}{\mathrm{RT}}$$

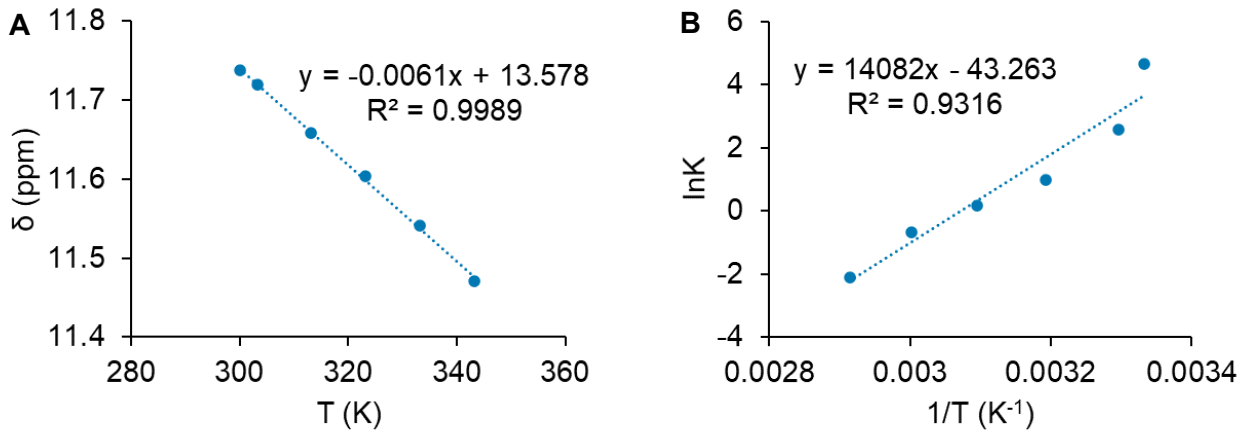


**Figure S23.** (A) Temperature dependence and (B) van't Hoff plots of the -OH peak of **2** at 1 mM from 27 °C to 70 °C.

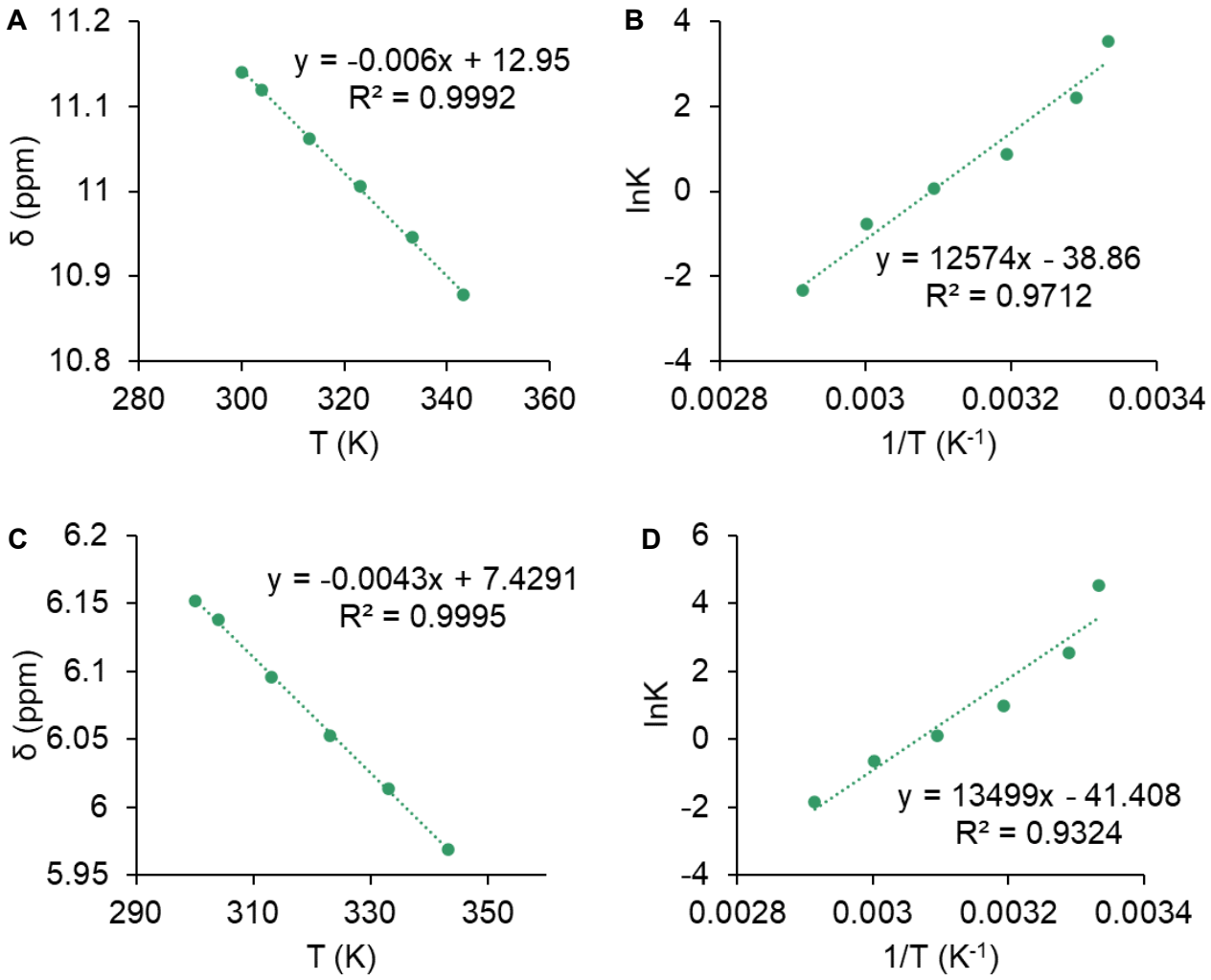


**Figure S24.** Temperature dependence and van't Hoff plots of the (A, B) -OH peak and (C, D) -NH peak of **3** at 1 mM from 27 °C to 70 °C.

**2D $^{1}$H-$^{1}$H NOESY**

NOESY experiments were carried out on 5.4 mM (2) or 5 mM (3) samples in a 5:4 mixture of DMSO-$d_6$:$C_6D_6$ on a 600 MHz instrument. The lack of NOEs in the spectrum of **2** (Figure S22) does not preclude intermolecular interactions in solution, but suggests that any intermolecular HB interactions that exist in solution must be with an aprotic heteroatom (i.e. phenazine N, C=O) or between intermolecular -OH groups.

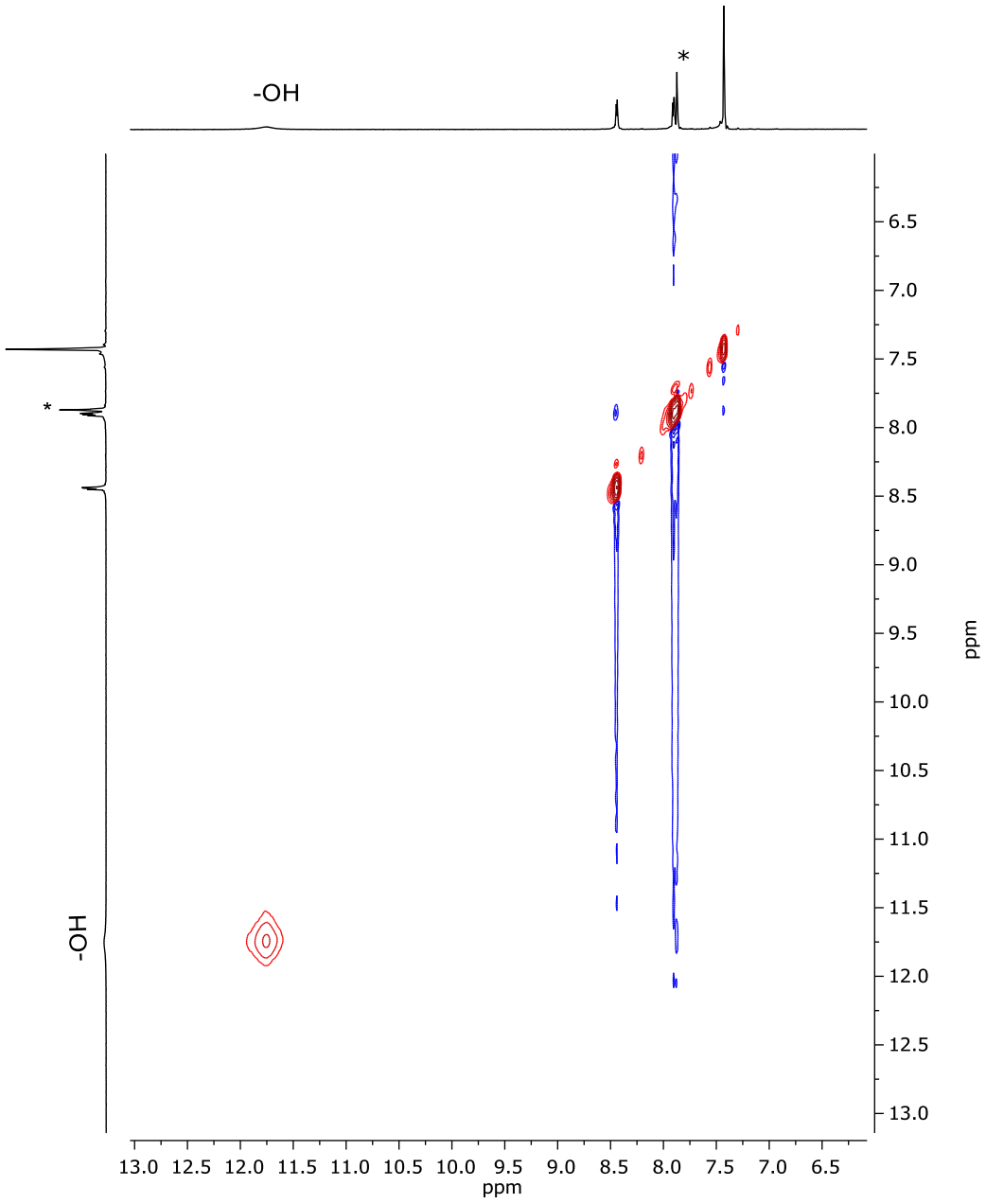


**Figure S25.** NOESY spectrum of **2** at 5.4 mM in 5:4 DMSO-$d_6$:$C_6D_6$. An asterisk marks the NMR solvent peak for $C_6D_6$.

**References**


(1) Miao, S.; Brombosz, S. M.; Schleyer, P. V. R.; Wu, J. I.; Barlow, S.; Marder, S. R.; Hardcastle, K. I.; Bunz, U. H. F. Are N,N-Dihydrodiazatetracene Derivatives Antiaromatic? *J. Am. Chem. Soc.* **2008**, *130*, 7339–7344. DOI:10.1021/ja077614p.

(2) Tang, Q.; Liang, Z.; Liu, J.; Xu, J.; Miao, Q. N-Heteroquinones: Quadruple Weak Hydrogen Bonds and n-Channel Transistors. *Chem. Commun.* **2010**, *46*, 2977. DOI:10.1039/c001215g.

(3) Chesneau, B.; Hardouin-Lerouge, M.; Hudhomme, P. A Fused Donor-Acceptor System Based on an Extended Tetrathiafulvalene and a Ruthenium Complex of Dipyridoquinoxaline. *Org. Lett.* **2010**, *12*, 4868–4871. DOI:10.1021/ol102022v.

(4) Manivannan, R.; Satheshkumar, A.; Elango, K. P. Tuning of the H-Bonding Ability of Imidazole N-H towards the Colorimetric Sensing of Fluoride and Cyanide Ions as Their Sodium Salts in Water †. *New J. Chem* **2013**, *37*, 3152. DOI:10.1039/c3nj00371j.

(5) Luo, Z.; Liu, L.; Zhao, Q.; Li, F.; Chen, J. An Insoluble Benzoquinone-Based Organic Cathode for Use in Rechargeable Lithium-Ion Batteries. *Angew. Chemie Int. Ed.* **2017**, *56*, 12561–12565. DOI:10.1002/anie.201706604.

(6) Manivannan, R.; Ciattini, S.; Chelazzi, L.; Elango, K. P. Benzoquinone-Imidazole Hybrids as Selective Colorimetric Sensors for Cyanide in Aqueous, Solid and Gas Phases. *RSC Adv.* **2015**, *5*, 87341–87351. DOI:10.1039/c5ra13597d.

(7) Toby, B. H.; Von Dreele, R. B. GSAS-II: The Genesis of a Modern Open-Source All Purpose Crystallography Software Package. *J. Appl. Crystallogr.* **2013**, *46*, 544–549. DOI:10.1107/S0021889813003531.

(8) Ge, Y.; Miller, L.; Ouimet, T.; Smith, D. K. Electrochemically Controlled Hydrogen Bonding. O-Quinones as Simple Redox-Dependent Receptors for Arylureas. *J. Org. Chem.* **2000**, *65*, 8831–8838. DOI:10.1021/jo000520c.

(9) Sivasankaran, U.; Vikraman, A. E.; Thomas, D.; Kumar, K. G. Nanomolar Level Determination of Octyl Gallate in Fats and Oils. *Food Anal. Methods* **2016**, *9*, 2115–2123. DOI:10.1007/s12161-015-0356-7.

(10) Cedano, M. R.; Smith, D. K. Redox-Responsive Dimerization in a Ferrocene-Ureidopyrimidone Supramolecular Assembly. *J. Org. Chem.* **2018**, *83*, 11595–11603. DOI:10.1021/acs.joc.8b01570.